BIOPHYSICS

Copper drives prion protein phase separation and modulates aggregation

Mariana Juliani do Amaral[1,2], Satabdee Mohapatra[2], Aline Ribeiro Passos[3], Taiana Sousa Lopes da Silva[1], Renato Sampaio Carvalho[1], Marcius da Silva Almeida[4]†, Anderson Sá Pinheiro[5]†, Susanne Wegmann[2]*, Yraima Cordeiro[1]*

Prion diseases are characterized by prion protein (PrP) transmissible aggregation and neurodegeneration, which has been linked to oxidative stress. The physiological function of PrP seems related to sequestering of redox-active Cu^{2+}, and Cu^{2+} dyshomeostasis is observed in prion disease brain. It is unclear whether Cu^{2+} contributes to PrP aggregation, recently shown to be mediated by PrP condensation. This study indicates that Cu^{2+} promotes PrP condensation in live cells at the cell surface and in vitro through copartitioning. Molecularly, Cu^{2+} inhibited PrP β-structure and hydrophobic residues exposure. Oxidation, induced by H_2O_2, triggered liquid-to-solid transition of PrP:Cu^{2+} condensates and promoted amyloid-like PrP aggregation. In cells, overexpression of PrP^C initially protected against Cu^{2+} cytotoxicity but led to PrP^C aggregation upon extended copper exposure. Our data suggest that PrP condensates function as a buffer for copper that prevents copper toxicity but can transition into PrP aggregation at prolonged oxidative stress.

INTRODUCTION

The prion protein (PrP) is highly expressed in neurons of the central nervous system. PrP is an extracellularly presented glycosylphosphatidylinositol (GPI)–anchored plasma membrane protein that is enriched at presynaptic sites, and about 10 to 20% of total PrP is found in the cytosol (*1*–*3*). In prion diseases, PrP undergoes self-propagating misfolding into a pathogenic β sheet enriched form that is associated with scrapie prion disease (PrP^{Sc}). Prion diseases are fatal and the only known transmissible proteinaceous diseases in humans and other mammals (*1*).

PrP^{Sc}-infected cell models and mice show metal ion (e.g., Cu^{2+}, Zn^{2+}, Fe^{2+}, and Mn^{2+}) dyshomeostasis and reduced cellular response to oxidative stress (*4*–*6*). Moreover, the lack of PrP^C in neurons from *prnp*-knockout mice leads to enhanced susceptibility to oxidative stress (*7*, *8*). Copper binding to PrP was described in vitro (*9*) and in vivo (*10*) and occurs with different affinities depending on Cu^{2+} availability, exhibiting positive (*10*) or negative cooperativity (*11*), which suggests a role of PrP as a Cu^{2+} buffering system (*9*, *12*) and in other biological functions (*13*). For example, PrP appears to facilitate the internalization of Cu^{2+} (*9*) and Zn^{2+} (*14*), whereby a reduction to Cu^{+} likely occurs in acidic endosomes (*9*, *15*). Furthermore, PrP has been suggested to "quench" redox activity of Cu^{2+} and other neurologically relevant transition metals (Fe, Zn, and Mn) (*16*–*18*).

The main Cu^{2+} binding activity is encoded in the PrP N-terminal domain whereby four histidine residues (H61, H69, H77, and H85; human protein residue numbering) within the octarepeat region (60 to 91; four PHGGGWGQ tandem repeats) and two nearby histidines (H96 and H111) coordinate copper ions (at pH ~ 7) (*18*). Recently, two C-terminal histidines, H140 and H177, were shown to cobind Cu^{2+}, thereby tethering PrP N- and C-terminal domains and promoting their interaction (*19*). In addition, H187 was also shown to coordinate Cu^{2+} (*20*). The Cu^{2+} coordinating octarepeat region of PrP was predicted to contain a distinctive uniform distribution of aromatic residues (*21*) and to form low-complexity amyloid-like kinked segments (LARKS) (*22*, *23*), which establish transient β sheet interactions and seem to be involved in driving liquid-liquid phase separation of low-complexity domains in proteins forming biomolecular condensates, e.g., membrane-less organelles. Protein condensates are dynamic liquid-like assemblies that can act as reaction hubs or structural entities, and contribute to the spatiotemporal organization of cellular processes (*24*, *25*). However, for proteins related to different neurodegenerative diseases, e.g., fused in sarcoma (FUS) and hnRNPA1 in amyotrophic lateral sclerosis (ALS), TAR DNA-binding protein 43 (TDP-43) in frontotemporal dementia and ALS, α-synuclein in Parkinson's disease, and Tau in Alzheimer's disease, a transition from liquid-like condensates to gel- or solid-like structures has been described and linked to their aggregation and neuropathological potential (*26*, *27*). PrP has been shown to undergo phase separation in vitro, modulated by nucleic acids, other proteins, and the physicochemical environment (*28*, *29*).

We hypothesized that Cu^{2+}, via its multivalent interactions with LARKS-containing octapeptide region and other domains of PrP, could promote physiological PrP condensation and even be involved in driving pathological PrP aggregation. Using a multiparametric biophysical and biochemical approach combining in vitro and live cell data, we revealed that Cu^{2+} promotes the condensation of recombinant PrP (PrP) in vitro, as well as membrane anchored PrP^C in cells. In vitro, Cu^{2+} together with hydrogen peroxide, mimicking oxidative stress, decreased the molecular diffusion inside PrP condensates, followed by a liquid-to-solid transition and the

[1]Faculdade de Farmácia, Universidade Federal do Rio de Janeiro, Rio de Janeiro, Brazil. [2]German Center for Neurodegenerative Diseases (DZNE), Berlin, Germany. [3]Brazilian Synchrotron Light Laboratory (LNLS), Brazilian Center for Research in Energy and Materials (CNPEM), Campinas, SP, Brazil. [4]Plataforma Avançada de Biomoléculas, Centro Nacional de Biologia Estrutural e Bioimagem, Instituto de Bioquímica Médica Leopoldo de Meis, Universidade Federal do Rio de Janeiro, Rio de Janeiro, Brazil. [5]Departamento de Bioquímica, Instituto de Química, Universidade Federal do Rio de Janeiro, Rio de Janeiro, Brazil.
*Corresponding author. Email: yraima@pharma.ufrj.br (Y.C.); susanne.wegmann@dzne.de (S.W.)
†These authors contributed equally to this work.

formation of amyloid-like PrP aggregates enriched in dityrosine cross-links. In cells overexpressing fluorescently labeled PrP^C, Cu^{2+} promoted the formation of membrane bound and cytoplasmic PrP^C condensates. PrP^C overexpression protected against Cu^{2+} cytotoxicity, indicating that PrP^C condensation may function as a copper buffering system by sequestering Cu^{2+} ions. Our data indicate that PrP condensation may be an integral mechanism for a variety of copper- and other metal ion–related functions, such as metal ion sensing, uptake, transport, and storage, which are important processes in signaling and oxidation protection. However, reactive oxygen species (ROS) production due to prolonged Cu^{2+} or H_2O_2 exposure can induce a liquid-to-solid transition of PrP:Cu^{2+} condensates, which can drive pathological PrP aggregation.

RESULTS

PrP^C undergoes membrane-associated condensation in cells

PrP^C is a cell surface protein that carries a GPI anchor on its C terminus, which is essential for the intracellular trafficking of PrP^C from the endoplasmic reticulum (ER) through the Golgi, and its anchoring to the outer leaflet of the plasma membrane (*30*). In vitro, recombinant PrP can form biomolecular condensates triggered by macromolecular crowding, nucleic acids, and protein interactors (Aβo, αSyn, and Tau) (*28*, *31*, *32*). Whether and where—at the membrane or in the cytosol—PrP^C forms condensates in the cellular environment is not known. In addition, it remains unclear what molecular partners, including metal ions, can modulate the liquid-liquid phase separation of PrP in living cells. To assess PrP^C phase separation, we used a construct containing PrP^C fused to yellow fluorescent protein followed by a GPI-anchor (PrP^C-YFP-GPI) and expressed it in human embryonic kidney (HEK) 293 cells.

Live cell confocal microscopy showed that most of PrP^C-YFP-GPI localized to the membrane (Fig. 1A, top left). PrP is a copper binding protein (*9*–*12*, *18*), and this metal ion up-regulates its expression (*33*). We found that treatment with 300 μM $CuCl_2$ (from here on: Cu^{2+}) for 1 hour appeared to increase the accumulation of PrP^C-YFP-GPI at the membrane, especially pronounced at the cell-cell interface, where the membranes of two adjacent cells expressing PrP^C-YFP-GPI were in contact (Fig. 1A, bottom left). Line plots across cell-cell interfaces and individual membranes of the same cells (examples in Fig. 1B) revealed a ~2-fold higher PrP^C-YFP-GPI fluorescence intensity at cell-cell interfaces (I_I) compared to the sum of the respective individual membranes ($I_{M1} + I_{M2}$), indicating a cooperative assembly of PrP^C-YFP-GPI at the interface of Cu^{2+}-treated cells [simple addition of PrP^C-YFP-GPI signal from adjacent membranes would give values of $I_I/(I_{M1} + I_{M2}) \leq 1$] (Fig. 1C). In untreated cells, the cell-cell interface had only 1.2-fold higher intensity indicating a less cooperative assembly for no Cu^{2+} versus Cu^{2+} ($P = 0.0001$). The PrP^C-YFP-GPI expression levels and absolute fluorescence intensity were similar between treated and untreated cells (fig. S1A). Cells expressing YFP-GPI did not show enrichment at the cell-cell interface (Fig. 1C).

Cooperative assembly is a characteristic of condensation, whereby proteins concentrate in a dense liquid-like phase. Proteins inside biomolecular condensates show a reduced molecular diffusion and a lower fraction of mobile molecules compared to freely diffusing cytosolic proteins, which can be observed as slower and/or less fluorescence recovery after photobleaching (FRAP). Condensates of membrane proteins show an additional FRAP delay because of restricted two-dimensional diffusion (*34*). To test whether Cu^{2+}-promoted enrichment of PrP^C-YFP-GPI at cell-cell interfaces is driven by condensation of extracellularly presented PrP^C, we compared FRAP of PrP^C-YFP-GPI in untreated and Cu^{2+}-treated cells (Fig. 1D). In response to Cu^{2+}, PrP^C-YFP-GPI showed significantly less recovery (no Cu^{2+}: ~70% versus Cu^{2+}: ~55%; $P = 0.0054$) indicating less mobile PrP^C species inside assemblies. FRAP of YFP-GPI was as expected for noncondensing membrane proteins and did not change by Cu^{2+} treatment (Fig. 1D). In contrast, individual cell membranes showed a high mobile population of PrP^C-YFP-GPI (~87%), as observed for YFP-GPI (~87%). Cu^{2+} treatment decreased the mobile species of PrP^C-YFP-GPI (no Cu^{2+}: ~87% versus Cu^{2+}: ~75%; $P = 0.0196$) at the same extent as for cell-cell interfaces (~15% less recovery for Cu^{2+} interfaces versus ~12% Cu^{2+} individual membranes; Fig. 1D), indicating that Cu^{2+} increases densely packed PrP^C. Together, these results suggest that PrP^C-YFP-GPI phase separates at cell-cell interfaces. Moreover, Cu^{2+} co-condensation occurs at the plasma membrane irrespective of site, as shown by the ~12 to 15% less recovery upon Cu^{2+} treatment in both individual cell membranes and cell-cell interfaces.

To further examine liquid-like characteristics of PrP condensates, we performed confocal time-lapse imaging. Both fusion and fission events of small PrP^C-YFP-GPI clusters occurred at the membrane, and Cu^{2+} promoted "puncta"-like structures in the plasma membrane (Fig. 1F and fig. S1D). Compared to green fluorescent protein (GFP), PrP^C-YFP-GPI–expressing cells showed a higher viability at increasing $CuCl_2$ concentrations in the culture medium (Fig. 1E and fig. S2, A, B, D, and E; $P = 0.0111$ at 600 μM and $P = 0.002$ at 1 mM $CuCl_2$), indicating that PrP^C exerted a protective effect against Cu^{2+}-induced cytotoxicity.

In addition to the plasma membrane–bound main pool, we observed a small fraction of PrP^C-YFP-GPI as highly mobile, small (diameter < 1 μm), round structures in the cytosol, often near the membrane (fig. S1D and movie S1), which is consistent with previously reported PrP^C puncta in hippocampal cells (*35*). Time lapse imaging showed coalescence of cytosolic PrP^C-YFP-GPI and the exchange of PrP^C-YFP-GPI signal between cytosolic structures and the membrane within seconds—in both directions (Fig. 1F, fig. S1D, and movies S1 and S2). These events are reminiscent of condensate fusion and fission. PrP^C-YFP-GPI cytosolic circular structures did not colocalize with membrane-bound organelles, i.e., endocytic compartments (fig. S3A), lysosomes (fig. S3B), and ER (fig. S3C), suggesting the absence of membranes around PrP^C-YFP-GPI condensates.

In some cells, we observed large accumulation of PrP^C next to the nucleus (fig. S1B), corroborant to previous observations on PrP overexpression (*36*), which may be related to misfolded protein accumulation at the aggresome (*2*). Notably, cells maintained in RPMI 1640 [containing 10% fetal bovine serum (FBS)], Opti-MEM, or imaging solution showed similar subcellular distribution of PrP^C-YFP-GPI (fig. S2C), and because 300 μM Cu^{2+} (for 1 hour) did not significantly impair cell viability, we used this condition for all experiments in Fig. 1. Collectively, our data suggest that the presence of Cu^{2+} enhances the accumulation of PrP^C at cell-cell interfaces driven by condensation and, simultaneously, reduces PrP^C molecular diffusion inside condensates. Sequestration of Cu^{2+} into PrP^C condensates might reduce oxidative stress, which

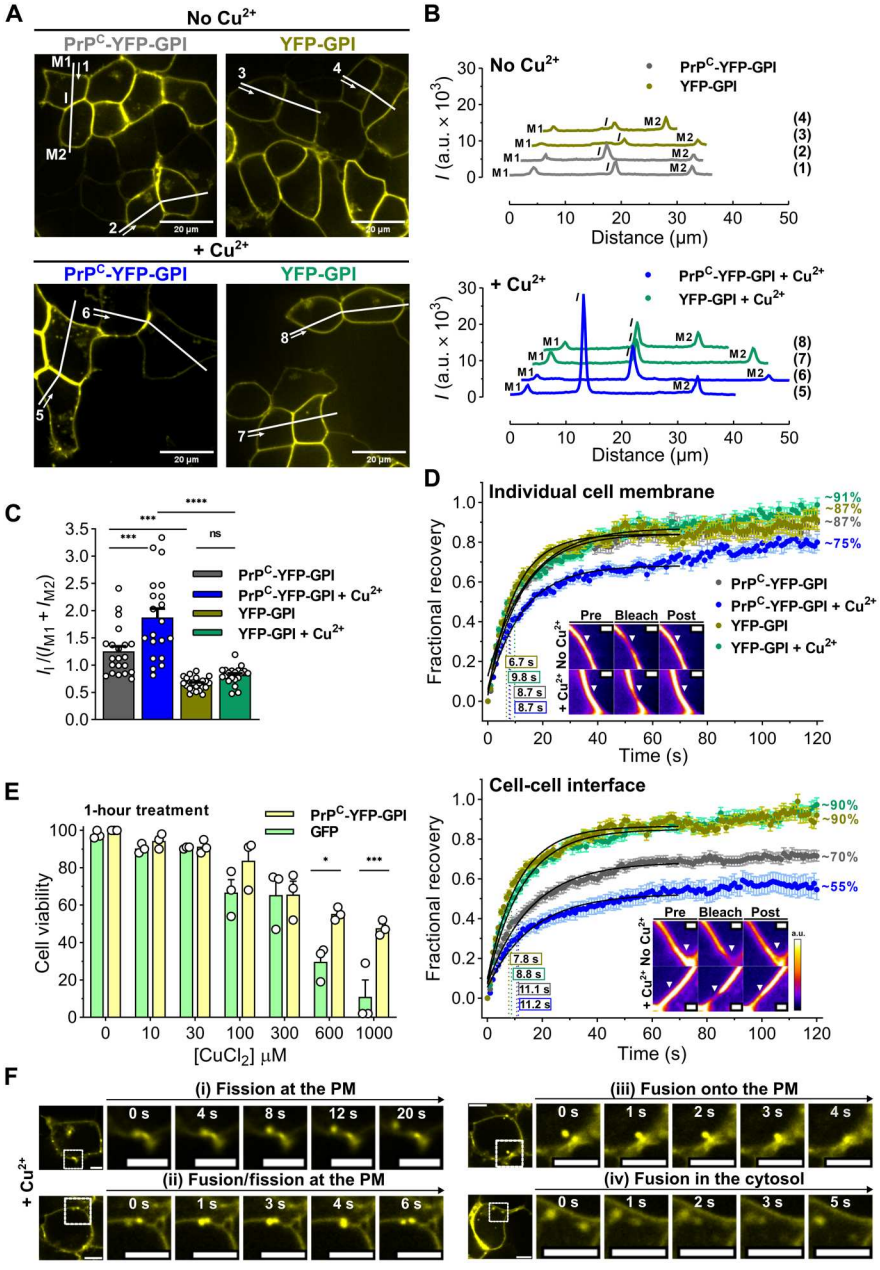

Fig. 1. PrP^C condensation at cell-cell contacts is promoted by Cu^{2+}. (**A**) Confocal images of HEK293 cells transfected with PrP^C-YFP-GPI or YFP-GPI showing localization at the plasma membrane and accumulation of PrP^C-YFP-GPI at cell-cell interfaces in untreated (top) or Cu^{2+}-treated (300 μM $CuCl_2$) cells (bottom). White lines across cell membranes (M1 and M2; not in contact with other cells) and interfaces (I) indicate positions and numbering of line plots in (B). Arrows mark the start and direction of measurement. (**B**) Line plots from (A) showing fluorescence intensity of individual membranes (M1 and M2) and the interface (I) of two adjacent cells treated with Cu^{2+} or not. (**C**) Fluorescence quantification at cell-cell interface relative to the sum of intensities measured for individual membranes of the contacting cells [$I_I/(I_{M1} + I_{M2})$]. Data shown as mean ± SEM, n = 20 to 23 measurements per group, one-way analysis of variance (ANOVA) (Tukey). ****$P < 0.0001$ and ***$P < 0.001$; ns, not significant. (**D**) FRAP shows a lower recovery of PrP^C-YFP-GPI at individual cell membranes or cell-cell interfaces upon Cu^{2+} treatment, indicating less molecular diffusion, as opposed to YFP-GPI with Cu^{2+} treatment or not. n = 23 to 26 bleached circular areas per group. Fitting to obtain times to half recovery ($t_{1/2}$; inside rectangles) are shown in black. Insets: Examples of bleached circular areas from PrP^C-YFP-GPI in the individual cell membranes (top) or interfaces (bottom). Pseudocolored intensity scale shown on the right. (**E**) Cell viability assay of HEK293 cells transfected with PrP^C-YFP-GPI or GFP treated with increasing concentrations of $CuCl_2$ for 1 hour. *$P < 0.05$ and ***$P < 0.001$. Data shown as mean ± SEM, n = 3 independent replicates, one-way ANOVA (Sidak). (**F**) Time-lapse confocal imaging of Cu^{2+}-treated cells showing liquid-like fission (i) and fusion (ii and iii) of small PrP^C-YFP-GPI clusters at the membrane or in the cytosol (iv). Time points indicated inside micrographs. Scale bars, 20 μm (A), 1 μm (D), and 5 μm (F). a.u., arbitrary units. PM, plasma membrane.

would explain the increased cell viability upon Cu^{2+} treatment in PrP^C-expressing cells.

Cu^{2+} triggers recombinant PrP condensation at physiological conditions in vitro

We proceeded to investigate the molecular mechanisms of Cu^{2+}-driven PrP condensation in vitro. Different bioinformatic prediction tools for the liquid-liquid phase separation propensity of proteins [Fuzdrop (*37*), catGRANULE (*38*), ParSe (*39*), and PScore (*40*)] agreed that the octarepeat region of PrP (residues 60 to 91), which binds Cu^{2+} ions via four histidine residues, has the highest probability to undergo phase separation (Fig. 2A), probably because of the five LARKS. PrP mutants with extra octarepeats that cause early-onset inherited prion diseases (*41*) showed enhanced phase separation propensities (fig. S4A), highlighting the relevance of this region for both phase separation and pathology and suggesting a modulation of PrP phase transitions by copper.

To examine how the binding of Cu^{2+}—the best-known function of the octarepeat region (*10*, *18*)—would modulate PrP condensation, we incubated recombinant PrP in physiological ion and molecular crowding conditions [physiological buffer (PhysB); including 6% polyethylene glycol (PEG)–4K; 25°C; Table 1] with different concentrations of $CuCl_2$ and monitored phase separation by microscopy (25 μM PrP; Fig. 2B) and turbidity (10 μM PrP; Fig. 2C). While PrP alone did not phase separate in these conditions, the addition of equimolar or higher amounts of $CuCl_2$ triggered the rapid formation of PrP condensates. PrP turbidity measurements indicated that phase separation plateaued at a PrP:Cu^{2+} molar ratio of 1:4 (Fig. 2C). Tryptophan fluorescence anisotropy confirmed the formation of higher-order oligomers or

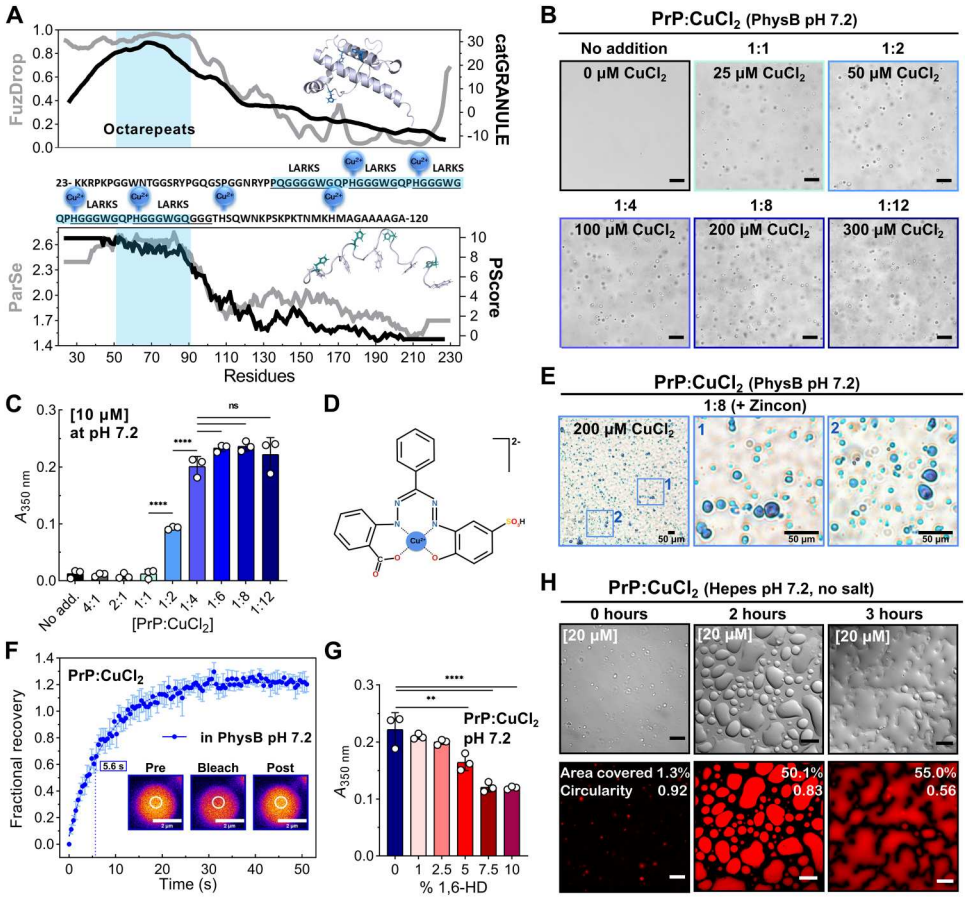

Fig. 2. Cu^{2+} drives recombinant PrP condensation. (**A**) Phase separation prediction of PrP (UniProt ID P04156) by FuzDrop (*37*) (top, gray line, left axis), catGRANULE (*38*) (top, black line, right axis), ParSe (*39*) (bottom, gray line, left axis), and PScore (*40*) (bottom, black line, right axis). Middle: Amino acid sequence of PrP N-terminal domain (23 to 120) with indicated copper-coordinating His. Five octarepeats (blue shading) are predicted to be LARKS. Top inset: PrP C-terminal domain structure (residues 121 to 231, PDB 1XYX) with Cu^{2+}-coordinating His side chains in blue. Bottom inset: Octarepeats structure (residues 23 to 106, PDB 2KKG) with evenly interspaced Trp (green) and Tyr (white) side chains that potentially contribute to phase separation. (**B**) Micrographs of PrP at 25 μM incubated for 2 hours with 25 to 200 μM $CuCl_2$. (**C**) Turbidity [absorption at 350 nm (A_{350} nm)] of 10 μM PrP at increasing $CuCl_2$ concentration. (**D**) Structure of Zincon:Cu^{2+} complex. (**E**) Microscopy images of 25 μM PrP with 200 μM $CuCl_2$ captured by a color high-resolution camera followed by Zincon addition. Zoomed-in of numbered regions are shown. (**F**) FRAP of 10 μM PrP (0.1% Alexa Fluor 647–labeled protein) with 80 μM $CuCl_2$ (1:8 molar ratio), performed immediately after sample preparation. Data shown as mean ± SEM (n = 3 condensates). Time to half recovery ($t_{1/2}$) is shown in the rectangle. (**G**) Turbidity of PrP:$CuCl_2$ (1:8 molar ratio) condensation upon increasing 1,6-HD concentrations (measured after 6 min). (**H**) Differential interference contrast (DIC) and fluorescence images of 20 μM PrP (0.1% Alexa Fluor 647–labeled protein) with 160 μM $CuCl_2$ (1:8 molar ratio) show wetting of poly-D-lysine–coated glass surfaces over time. Data in (C) and (G) shown as mean ± SD (n = 3), one-way ANOVA (Tukey). ****P < 0.0001 and **P < 0.01. Scale bars, 20 μm (B and H), 50 μm (E), and 2 μm (F).

Table 1. Composition of the physiological buffer used in this study and relevant physiological concentrations of copper ions reported in the literature. PhysB, physiological buffer.

PhysB	
Salt	***Concentration***
Hepes pH 7.2*	10 mM
KCl	120 mM
NaCl	5 mM
$CaCl_2$	150 μM
$MgCl_2$	5 mM
PEG4K	60 mg/ml (=6%, w/v)
Copper ions	
Location	***Concentration***
Cerebrospinal fluid	~70 μM (*86*)
Human brain	~80 μM (*87*)
Locus coeruleus	~860 ng/mg of wet tissue (*88*)
Substantia nigra	1200 ng/mg of wet tissue (*88*)
Synaptic cleft	100–250 μM (*86*)
	200–400 μM (*89*)
Synaptic vesicle	~291 μM (*89*)
Synaptosome	~48 μM (*89*)
	~15 μM (*90*)

*Replaced to K_2HPO_4/KH_2PO_4 in some experiments due to technical hindrance. Buffer composition was adapted from the "cytomix" buffer (*91*, *92*) together with findings on the ionic composition, and the pH values reported for mammalian cells and reviewed in (*93*).

condensates at PrP:Cu^{2+} molar ratios of 1:4 and 1:8 (fig. S4B). At pH 4.7, when the octapeptide histidine residues are protonated and metal coordination is negligible (*42*), no condensation occurred (fig. S4C), even with higher molecular crowding (10% PEG4K or PEG20K) (fig. S4D) or low temperature (fig. S4E, top image). Notably, at nonphysiological conditions of high protein concentrations (~70 μM at ~13°C; fig. S4G), very high molecular crowding (10% PEG20K; fig. S7, C and D), and low temperatures (25 μM at ~10°C; fig. S4, E and F), we were able to observe "homotypic" condensation for PrP alone, which seemed to be inhibited at low pH 4.7 (fig. S4, C to E) and promoted by high NaCl (300 to 500 mM) in the buffer (fig. S4G).

To ascertain whether Cu^{2+} ions are partitioning into condensates, we used the dye Zincon (Fig. 2D) (*43*). Microscopy (Fig. 2E) and spectrophotometric quantification of the dense phase with Zincon revealed that Cu^{2+} ions enriched at least 10-fold in the PrP:Cu^{2+} condensates (fig. S5). To test whether the Cu^{2+} in the condensates was essential for their stability, we added EDTA to preformed PrP:Cu^{2+} condensates, expecting this chelator would dissolve the condensates by complexing Cu^{2+} necessary for condensation. Turbidity measurements suggested that EDTA dissolved PrP:Cu^{2+} condensates within a few minutes (fig. S6A). Microscopy showed the formation of larger vacuolated intermediates that gradually dissolved (fig. S6B). Likewise EDTA, tris coordinates Cu^{2+} ions (*44*) and has been shown to outcompete Cu^{2+} binding to octarepeat peptides derived from PrP (*45*). Compared to "Cu^{2+} non-coordinating" Hepes buffer (*46*), six times less PrP:Cu^{2+} condensates were observed in tris buffer (fig. S6, C to E).

We further investigated the conditions at which Cu^{2+}-induced PrP condensation would occur. At a fixed, physiological relevant concentration of $CuCl_2$ (80 μM; Table 1), liquid-liquid phase separation depended on PrP concentration and started at 4 μM PrP (fig. S7A). Next, we used a bis-glycine complex [$Cu(Gly)_2$] as source of Cu^{2+} ions to resemble the cellular milieu, in which Cu^{2+} is mostly found protein-bound. Even in the $Cu(Gly)_2$ form, Cu^{2+} was able to induce PrP liquid droplets (fig. S7B). In the same experiment, we also observed the dependence of PrP:$Cu(Gly)_2$ phase separation on increasing molecular crowding (% PEG4K), indicating a synergy between Cu^{2+} and molecular crowding in driving PrP phase separation (fig. S7B). The amount of molecular crowding induced by PEG with different molecular weights (fig. S7, C to F) appeared to influence the surface attachment (fig. S7E) and shape of PrP:Cu^{2+} condensates (fig. S7F).

Altogether, these data show that Cu^{2+} is a major modulator of PrP phase separation, confirming our observations made for PrP^C in cells. PrP:Cu^{2+} condensation occurs at physiological PrP, copper, pH, salt, and crowding conditions.

PrP:Cu^{2+} condensation is promoted at low temperature and higher crowding and is mostly electrostatically driven

We sought to understand which molecular interactions would drive and stabilize PrP:Cu^{2+} condensates. FRAP suggested liquid-like molecular diffusion of PrP inside condensates (Fig. 2F). Turbidity temperature ramping experiments (between 13° and 40°C) showed that Cu^{2+}-induced PrP condensation increased with decreasing temperatures, starting at ~24°C, which was fully reversible upon reheating the sample (fig. S8A). Dynamic light scattering (DLS) confirmed that the majority of PrP:Cu^{2+} condensates were larger at 20°C (hydrodynamic radius, R_h ~ 540 nm) than at 37°C (R_h ~ 340 nm) (fig. S8B), corroborating the induction of PrP condensation at lower temperatures (fig. S8A). Notably, in PhysB (contains 6% PEG4K as crowding agent), a small amount (mass percentage < 1%) of multimers occurred (fig. S8B).

Protein condensation is driven by weak multivalent intra- and intermolecular interactions between residue side chains and protein structural elements, and clients (e.g., proteins, nucleic acids, or ions) can modulate these contacts (*31*). To test whether hydrophobic interactions stabilize PrP:Cu^{2+} condensates, we added the aliphatic alcohol 1,6-hexanediol (1,6-HD) to preformed PrP:Cu^{2+} condensates. 1,6-HD was reported to dissolve condensates of $PrP^{90–231}$ (residues 90 to 231) at 10% (w/v) (*29*), and of PrPY145Stop (residues 23 to 144) (*47*) at 2% (w/v), highlighting the role of weak hydrophobic contacts in homotypic liquid-liquid phase separation (LLPS) of these constructs. For Cu^{2+}-driven PrP LLPS, we observed only a 45% decrease in turbidity at 10% 1,6-HD and no effect at 2% 1,6-HD (Fig. 2G). We concluded that hydrophobic interactions have a smaller contribution to PrP:Cu^{2+} LLPS, and electrostatic interactions may play an important role. In the absence of counter ions in the buffer that weaken electrostatic interactions [10 mM Hepes, (pH 7.2), no salt], Alexa Fluor 647–PrP:Cu^{2+} condensation was enhanced, and pronounced wetting of positively charged (poly-D-lysine–coated) glass surfaces occurred (Fig. 2H and movie S3). A similar behavior was observed for electrostatically driven coacervates of Tau (*48*).

We probed Cu^{2+}-induced conformation changes at the same conditions of our phase separation assessment. By circular dichroism (CD) spectroscopy using PrP concentrations (2.5 μM) below the critical concentration for condensation to avoid light scattering artifacts, we observed minor increase of α-helical content (indicated by the 222- and 208-nm bands) upon Cu^{2+} addition (fig. S8C). Intrinsic tryptophan fluorescence showed quenching as a function of [$CuCl_2$] (fig. S8D), indicative of Cu^{2+}-induced structural changes and/or binding near tryptophan residues. The affinity of Cu^{2+} toward PrP in PhysB (fig. S8D, inset) supported previous results (i.e., dissociation constant K_D ~ 3 to 12 μM) (*9*, *11*, *49*). These data suggest that Cu^{2+}- driven phase separation is not followed by significant secondary/tertiary structural changes. However, it is important to note that long-range interactions between the N- and the C-terminal domains of PrP are promoted by Cu^{2+} leading to overall compaction, as observed in high-resolution structural studies (*19*, *50*).

Divalent/trivalent metal ions trigger PrP phase transitions

Given that PrP^C binds other divalent metal ions and regulates their homeostasis (*6*), we investigated how $FeCl_2$, ferric ammonium citrate (FAC), $ZnCl_2$, $CoCl_2$, $CdCl_2$, and $MnCl_2$ would modulate PrP condensation. Phase contrast microscopy and turbidity measurements showed that $FeCl_2$, FAC, $ZnCl_2$, $CdCl_2$, and $MnCl_2$ trigger PrP phase separation (fig. S9). Copper(II) sulfate ($CuSO_4$) promoted PrP phase separation like $CuCl_2$; hence, Cu^{2+} effect on phase separation is not dependent on the type of salt counter anion (fig. S9, A to C). $ZnCl_2$ only triggered PrP phase separation at higher molar ratios (1:8) and not at equimolarity like $CuCl_2$ or $CuSO_4$, $FeCl_2$, and FAC. $CdCl_2$ and $MnCl_2$ led to few micron-sized liquid-like droplets by microscopy, albeit the increase of turbidity. Both divalent (Fe^{2+} and $FeCl_2$) and trivalent (Fe^{3+} and FAC) iron drove PrP phase separation, whereas $CoCl_2$ did not trigger PrP phase separation at the conditions tested. It is worth noting that Cu^{2+}, Fe^{2+}/Fe^{3+}, Zn^{2+}, Co^{2+}, and Mn^{2+} are essential trace elements in the nervous system, especially in the synaptic cleft (*6*, *13*). We speculate that synaptic PrP condensates could act as a buffer for regulating the concentration of divalent metal ions at synapses.

H_2O_2 promotes a liquid-to-solid transition of PrP:Cu^{2+} condensates

Cu^{2+} is redox active and can engage with hydrogen peroxide (H_2O_2) in Fenton reaction, generating ROS. Since PrP:Cu^{2+} complexes can encounter H_2O_2 intra- and extracellularly to generate ROS, we investigated the effect of H_2O_2 on PrP phase transitions. Adding 10 mM H_2O_2 to PrP:Cu^{2+} phase separation conditions produced a mix of condensates and branched aggregates at all PrP:Cu^{2+} molar ratios after 2 hours, most pronounced at higher copper concentrations (Fig. 3, A to C, and fig. S10, A and B). H_2O_2 alone did not trigger PrP condensation or aggregation (fig. S11B). Condensates adhered to the branches of aggregates were visualized (Fig. 3C). Turbidity measurements of PrP:Cu^{2+} upon H_2O_2 addition led to significantly stimulated phase separation at 1:1 and 1:2 PrP:Cu^{2+} molar ratios as compared to the absence of H_2O_2 [PrP:Cu^{2+}, (1:1): $P < 0.05$; (1:2): $P < 0.001$; Fig. 3B and fig. S11C]. Aggregates occurring in [PrP:Cu^{2+} + H_2O_2] samples had solvent-exposed hydrophobic residues, revealed by SYPRO orange binding (Fig. 3C), and showed intrinsic fluorescence upon excitation in the ultraviolet (UV) range, suggesting amyloid-like cross–β sheet structure (Fig. 3D) (*51*). After 24 hours, amorphous and fibrillar aggregates could be observed (fig. S11A). FRAP in Hepes buffer (without salt) showed ~60% recovery for PrP:Cu^{2+} condensates [half-time ($t_{1/2}$) ~ 13.3 s] versus no recovery for [PrP:Cu^{2+} + H_2O_2] condensates/aggregates (Fig. 3E and fig. S10D), indicating loss of molecular diffusion. Notably, PrP:Cu^{2+} recovery was slower than in PhysB ($t_{1/2}$ ~ 5.6 s; PhysB contains 120 mM KCl and higher ionic strength, see Table 1) (Fig. 2F), suggesting less molecular diffusion inside PrP:Cu^{2+} condensates when electrostatic interactions are favored (fig. S10C).

X-ray photon correlation spectroscopy reveals H_2O_2-induced differences in PrP:Cu^{2+} condensates material properties

Biomolecular condensates are metastable complex fluids that can become less dynamic over time (*52*, *53*). To gain further insights into the effect of H_2O_2 on PrP:Cu^{2+} condensate fluidity, we assessed the dynamic properties of a fluid or polymer over the time (microseconds to hours) and length (nanometers to micrometers) scales relevant for phase separation using x-ray photon correlation spectroscopy (XPCS) (*54*, *55*). Both PrP:Cu^{2+} and [PrP:Cu^{2+} + H_2O_2] displayed a single exponential decay and dynamics in the range of seconds (Fig. 3F). The broad exponential decay of the autocorrelation functions indicated dynamical heterogeneities observed in viscous systems (*56*). PrP:Cu^{2+} condensate relaxation dynamics were characterized by subdiffusive motion ($\gamma < 1$; for comparison: $\gamma = 1$, Brownian motion; $\gamma > 1$, superdiffusive) over the entire dynamic size scale (acquisition q-range; Fig. 3G and fig. S11D). Slow, subdiffusive relaxation is observed in the coarsening of viscous condensates (*56*), e.g., during phase separation of lysozyme (*55*). PrP:Cu^{2+} condensates have characteristics of a viscous fluid that can transition into soft glassy materials, reminiscent of condensates formed by the FUS protein that display an increase in viscosity but no change in elasticity over time, described as aging Maxwell fluids (*53*). FUS condensates do not show morphological changes during aging likewise PrP:Cu^{2+} condensates after 24 hours (fig. S11E), albeit the observed rheological changes in FUS (*53*). However, when adding H_2O_2, we observed remarkable changes in the dynamic properties of condensates (Fig. 3G). The [PrP:Cu^{2+} + H_2O_2] condensates/aggregates were characterized by superdiffusive ($\gamma > 1$) viscoelastic relaxation indicating network fluctuations in the condensates, likely via liquid-to-solid transition during gelation/hardening (*54*, *55*). The loss of molecular diffusion (FRAP data, Fig. 3E) and progressive formation of aggregated structures (microscopy data shown in Fig. 3, A, C, and D, and fig. S11A) support this idea.

Cu^{2+} prevents PrP misfolding but in the presence of H_2O_2 triggers amyloid formation

To further assess the influence of Cu^{2+} and H_2O_2 on PrP aggregation, we performed in vitro aggregation assays by seeding PrP with preformed recombinant PrP fibrils produced under denaturant condition (*57*), in the absence or presence of $CuCl_2$ and/or H_2O_2 (Fig. 4A). This condition would mimic a pathological condition with seeded polymerization of PrP^C and oxidative stress ($CuCl_2$ + H_2O_2).

DLS showed a multimodal particle size distribution for all samples after the aggregation assay, and at least 30% of particles were composed by multimers (R_h ranging from 180 to 863 nm)

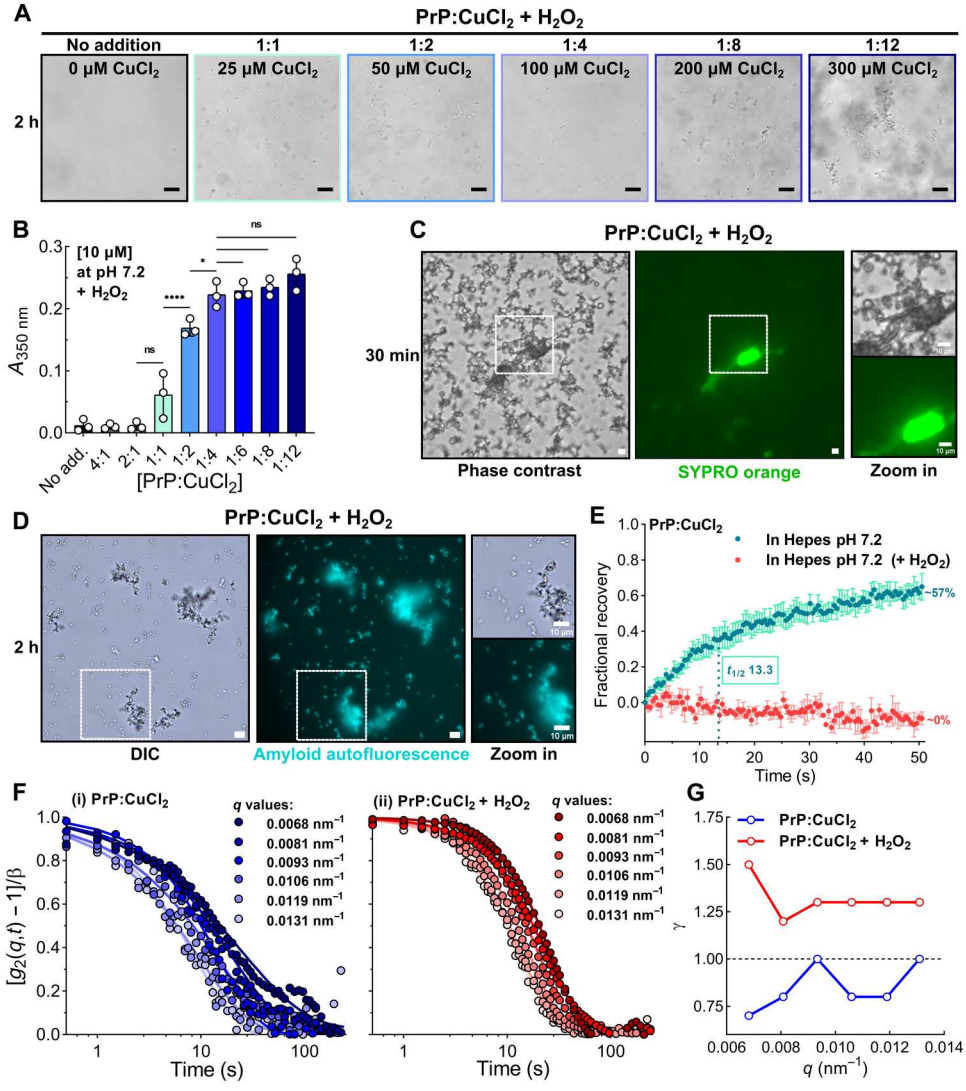

Fig. 3. H_2O_2 treatment triggers PrP:Cu^{2+} liquid-to-solid phase transition. (**A**) Phase contrast images of 25 μM PrP incubated with increasing concentrations of $CuCl_2$ in the presence of 10 mM H_2O_2 (2-hour incubation). (**B**) Turbidity (A_{350} nm) of 10 μM PrP at increasing $CuCl_2$ concentrations (6 min after sample preparation) in the presence of H_2O_2. Data shown as mean ± SD, $n = 3$. (**C**) Phase contrast (left) and fluorescence (right) images of 25 μM PrP with 200 μM $CuCl_2$ and 10 mM H_2O_2, stained with SYPRO orange after 30 min. Zooms of marked regions are shown on the right. (**D**) DIC (left) and fluorescence (right; intrinsic blue fluorescence characteristic of amyloids) images of 25 μM PrP incubated with 200 μM $CuCl_2$ and 10 mM H_2O_2 after 2-hour incubation. Marked regions are zoomed. (**E**) FRAP of 10 μM PrP with 80 μM $CuCl_2$ in 20 mM Hepes (pH 7.4) (green; $t_{1/2}$ in seconds is shown in the rectangle) and upon addition of 10 mM H_2O_2 (red). FRAP recorded immediately after sample preparation. Data shown as mean ± SEM, n = 3 condensates. (**F**) XPCS autocorrelation functions for increasing q values of PrP:Cu^{2+} (i) and PrP:Cu^{2+} + H_2O_2 (ii). (**G**) XPCS-derived Kohlrausch-Williams-Watts (KWW) exponent, γ, over the recorded q range for PrP:Cu^{2+} (blue) and PrP:Cu^{2+} + H_2O_2 (red). All experiments were performed at 25°C in PhysB, unless otherwise stated. Scale bars, 20 μm (A) and 10 μm (C and D).

(Fig. 4B). Notably, monomeric PrP not subjected to the aggregation protocol has a R_h of ~2.2 nm (fig. S8B). Addition of $CuCl_2$ or $CuCl_2$ + H_2O_2 resulted in the lack of monomeric or low-order PrP species (for monomer up to tetramer; R_h ranges from 2.2 to 20 nm, considering the partially unfolded nature of PrP), suggesting a shift to multimers of PrP. The PrP:H_2O_2 sample did not show large particle formation. Oppositely, the PrP:Cu^{2+} + H_2O_2 sample showed the highest mass of multimers (R_h > 800 nm) (Fig. 4B). Therefore, the enhanced phase transition of [PrP:Cu^{2+} + H_2O_2] may synergize with seeded aggregation of PrP. We then proceeded the characterization of PrP aggregates by transmission electron microscopy (TEM). PrP and PrP:H_2O_2 formed similar clusters of amorphous aggregates (Fig. 4C). PrP:$CuCl_2$ formed circular structures reminiscent of condensates, few small amorphous aggregates, and diffuse material that may correspond to soluble oligomers (Fig. 4C, blue arrowheads). In PrP:Cu^{2+} + H_2O_2 preparations, we detected several branched aggregates as well as long fibrils and clusters of amorphous aggregates with weaved-in circular condensate-like structures (Fig. 4C).

To explore whether the aggregates observed by TEM contained amyloid-like β-structure, we measured SYPRO orange fluorescence emission (Fig. 4D). SYPRO orange binds to unfolded hydrophobic

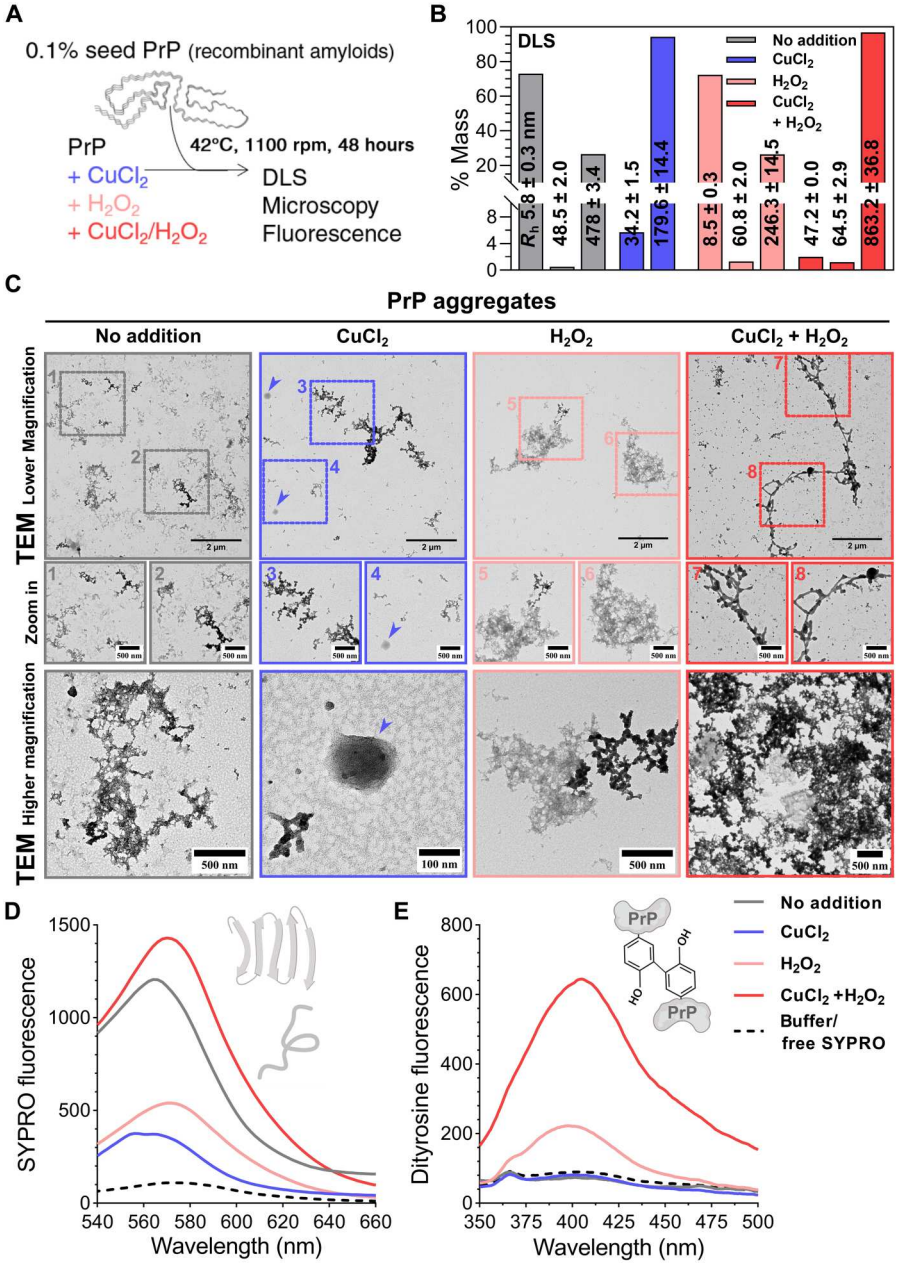

Fig. 4. Cu^{2+} reduces PrP misfolding and, together with H_2O_2, results in dityrosine-rich PrP aggregates. (**A**) Experimental setup to examine PrP seeded aggregation in vitro. PrP (25 μM) was incubated with 0.1% seeds (pre-aggregated PrP obtained from denaturation protocol with 1 M guanidinium-HCl, 3 M urea) under continuous agitation at 42°C for 48 hours in the presence or absence of $CuCl_2$ (200 μM), H_2O_2 (10 mM), or both. (**B**) DLS analysis of aggregated 48-hour samples (diluted to 1 μM for measurements). Mass percentage of each species is plotted, and R_h is shown within bars. Data shown as mean ± SD from 10 acquisitions at 25°C. (**C**) Negative-stain TEM at different magnifications. Blue arrowheads indicate circular condensate-like structures. Zoom-in of numbered regions are shown in the middle. (**D**) SYPRO orange emission spectra (excitation, 495 nm; emission, 535 to 665 nm) of 48-hour aggregated samples. The illustrations show a β sheet–rich structure and an unfolded protein, which are probed by SYPRO orange. (**E**) Dityrosine intrinsic fluorescence (excitation, 325 nm; emission, 350 to 500 nm) of 48-hour aggregated samples. Intramolecular (between two vicinal tyrosine residues) and intermolecular (inset illustration) dityrosine cross-links can be formed in oxidative conditions (catalyzed by Cu^{2+}/H_2O_2). Legend applies to (D) and (E). All samples were prepared in PhysB pH 7.2. Scale bars are indicated inside images.

protein surfaces, and it has been shown ~3-fold more sensitivity than thioflavin T (ThT) for amyloid quantification (*58*). PrP:Cu^{2+} + H_2O_2 samples showed the highest SYPRO fluorescence intensity, followed by PrP alone, indicating misfolding and/or amyloid-like characteristics in these samples. PrP:Cu^{2+} and PrP:H_2O_2 had similar low SYPRO intensities (Fig. 4D). Notably, SYPRO fluorescence of PrP:$CuCl_2$ showed an 8-nm blue shift of the maximum emission wavelength (λ_{max} = 556 nm for PrP:$CuCl_2$ versus 564 nm for PrP), indicating a more hydrophobic environment. Measuring the fluorescence of 1-anilino-8-naphthalenesulfonate (1,8-ANS), whose fluorescence intensity is enhanced in hydrophobic environments, confirmed this observation (fig. S12, A and B). After 48 hours of incubation with preformed PrP seeds, PrP but not PrP:$CuCl_2$ showed enhanced 1,8-ANS fluorescence (fig. S12B), indicating that Cu^{2+} prevented the exposure of hydrophobic residues due to partial unfolding of PrP. Furthermore, ThT aggregation kinetics showed a typical sigmoidal curve for PrP aggregation ($t_{1/2}$ = 35.3 hours). However, PrP:Cu^{2+} showed no binding to ThT over 72 hours (fig. S12C), corroborating the absence of amyloid aggregates in this sample. In summary, our results including DLS, TEM, and binding to amyloid dyes suggest that H_2O_2 promotes PrP amyloid formation only in the presence of $CuCl_2$, whereas Cu^{2+} alone prevents organized aggregates formation.

We wondered what would be the mechanism by which $CuCl_2$ together with H_2O_2 elicit PrP aggregation. First, to determine changes in protein folding that could favor PrP aggregation, we measured intrinsic tryptophan fluorescence during thermal denaturation, right after sample preparation (fig. S13). PrP conformation was significantly affected by $CuCl_2$ + H_2O_2, even at room temperature, evident from a ~fourfold decreased fluorescence intensity (versus PrP; fig. S13, D and E). In addition, the emission spectrum exhibited a red shift (fig. S13, D and F), possibly due to dityrosine formation (emission at 405 nm).

In metal-catalyzed oxidation conditions (e.g., $CuCl_2$ + H_2O_2), covalent intra- and intermolecular cross-links that promote protein aggregation can occur through dityrosine formation (*59*). We investigated whether H_2O_2 would trigger dityrosine formation in PrP, which is apparent from an increase in dityrosine fluorescence. The presence of $CuCl_2$ + H_2O_2 significantly increased dityrosine formation in PrP aggregates compared to all other conditions, e.g., threefold increased emission at 405 nm compared to PrP:H_2O_2 (Fig. 4E). Eleven of 13 tyrosine residues are in the C-terminal half of PrP that forms the protease and denaturation-resistant core of pathological PrP aggregates (*1*), likely explaining why oxidation-induced dityrosine cross-linking favors PrP aggregation. Cryo–electron microscopy (cryo-EM)–derived structures of 263 K, aRML, wtRML, and a22L prion fibrils [Protein Data Bank (PDB) IDs: 5o3l, 7qig, 7lna, and 8efu] (*60*) suggest the potential for establishing cross-links between closely positioned pairs of tyrosine residues. Although dityrosines were not observed in these cryo-EM models, tyrosine rings might adopt ortho-ortho conformation to form cross-links.

In addition to dityrosines, ROS produced by Fenton reactions, as catalyzed by Cu^{2+} + H_2O_2, induces pathological "β-cleavage" of PrP^C around residue 90, releasing the N-terminal domain extracellularly while keeping the C-terminal domain attached to the cell surface (*61*, *62*). We evaluated whether recombinant PrP with $CuCl_2$ + H_2O_2 would undergo β-cleavage in vitro (fig. S14). SDS–polyacrylamide gel electrophoresis (SDS-PAGE) showed that [PrP:$CuCl_2$ + H_2O_2] samples contained full-length PrP (~22 kDa) and SDS-stable higher-order oligomers right after sample preparation (fig. S14B, first lane). After 30 min, these PrP species started to disappear, and a 15- to 20-kDa fragment appeared (~16.3 kDa; arrow; fig. S14B), likely corresponding to the C-terminal product of β-cleavage. After 120 min, ~75% of full-length PrP and the C-terminal fragments were degraded in PrP:$CuCl_2$ + H_2O_2 (fig. S14C). In summary, the presence of copper in oxidative condition ($CuCl_2$ + H_2O_2) seems to trigger PrP aggregation via multiple mechanisms, including PrP unfolding and exposure of hydrophobic residues, production of the aggregation-prone C-terminal fragment through β-cleavage, and the formation of dityrosine cross-links.

Extended exposure to Cu^{2+} induces intracellular PrP aggregation

We asked whether $CuCl_2$ and ROS would also induce PrP aggregation in cells, for example, promoted by PrP oxidation and/or β-cleavage. Because cellular systems naturally have H_2O_2 and other ROS as metabolism by-products, Cu(II)/(I) can catalyze further ROS production by intra- and extracellular Fenton reactions. We incubated HEK293 cells expressing PrP^C-YFP-GPI with 300 μM $CuCl_2$ for 3 hours (notably, experiments presented in Fig. 1 were conducted within 1 hour) and tested the formation of amyloid-like aggregates by addition of amyloid dyes. Cu^{2+} exposure for 3 hours led to AmyTracker680-positive aggregates at the cell surface (Fig. 5, A and B). In addition, we observed the formation of vesicle-like hollow, spherical structures in the cytosol that carried PrP^C-YFP-GPI in their surrounding membrane (Fig. 5C and movie S4). We speculate that these structures might be stress-induced ER vesicles (*63*). When incubating cells with $CuCl_2$ in serum-free imaging solution [lacking ROS scavenging proteins like albumin (*64*)], we observed PrP^C-YFP-GPI signal near the nucleus and Nile Red–positive PrP aggregates (fig. S15, A and B). Notably, HeLa cells transfected with PrP^C-YFP-GPI incubated with $CuCl_2$ showed hollow spherical ER-like structures already after 1 hour, indicating that these cells might be more vulnerable to PrP:$CuCl_2$-induced conditions (fig. S15C). These data corroborate the observed amyloid-like aggregates of [PrP:$CuCl_2$ + H_2O_2] (Figs. 3 and 4), indicating that oxidative stress promotes PrP liquid-to-solid transition in vitro and in celullo.

DISCUSSION

In the last 25 years, it became clear that PrP plays a key role on copper homeostasis (*10*, *18*) and that, in turn, copper influences PrP aggregation (*13*, *50*, *65*). With our data, we now provide mechanistic evidence that both observations are related to PrP liquid-liquid phase separation and its modulation by Cu^{2+}. Earlier works showed PrP (protein domains or mutants) in vitro phase separation in simple buffer systems and without consideration of physiological Cu^{2+} concentration (*28*, *29*, *47*, *66*–*68*). By investigating the effects of Cu^{2+} on full-length PrP condensation and aggregation at physiologically relevant PrP concentrations [4 μM (*28*)], ionic strength, pH, and molecular crowding, we not only complement previous studies but are able to provide evidence for the role of PrP:Cu^{2+} condensation in the cellular context.

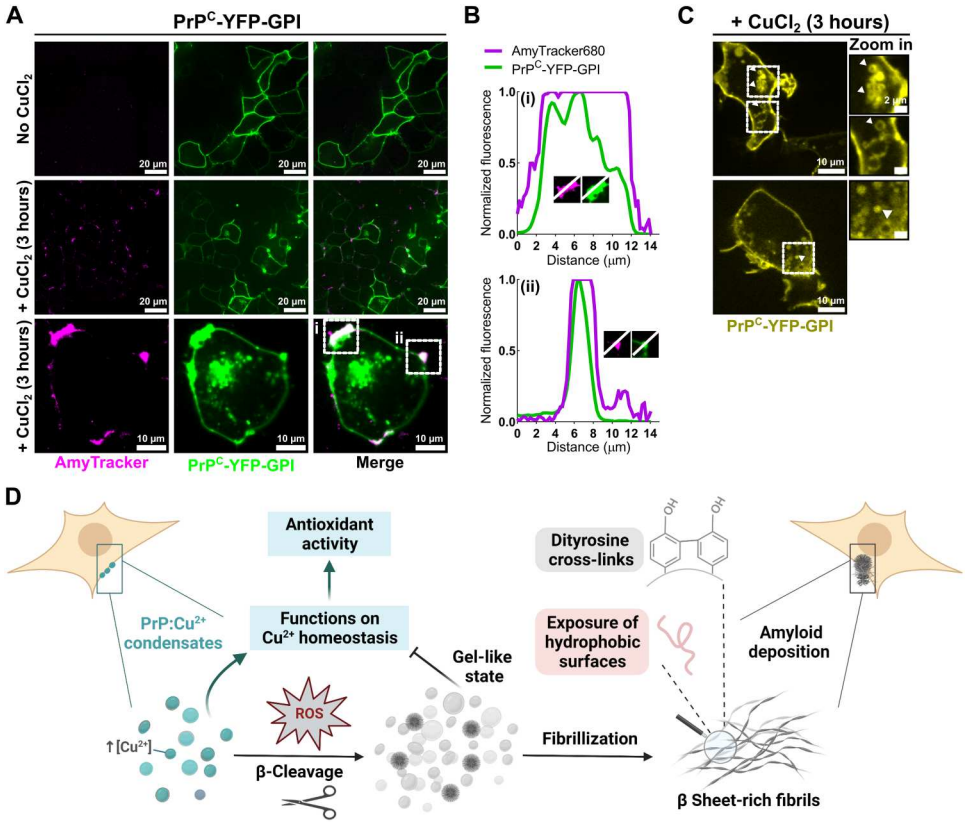

Fig. 5. Long-term exposure to Cu^{2+} leads to PrP^C-YFP-GPI amyloid-like aggregates in cells. (**A**) Live cell imaging of HEK293 cells transfected with PrP^C-YFP-GPI. Cells treated with 300 μM $CuCl_2$ for 3 hours (middle and bottom rows) showed AmyTracker680-positive aggregates at the cell surface. Bottom: Individual cell with PrP aggregates. White lines indicate positions of line profiles shown in (B). (**B**) Line profiles through AmyTracker-positive PrP aggregates at the surface of the cell shown in (A, bottom). (**C**) Formation of spherical hollow structures with PrP^C-YFP-GPI in the surrounding membrane after 3 hours of Cu^{2+}-treatment. Zoom-in of marked regions are shown on the right. (**D**) Schematic diagram on the role of copper in PrP^C condensation and oxidation-induced aggregation. PrP:Cu^{2+} condensation at the cell surface buffers Cu^{2+} concentration by sequestering redox-active excessive copper. This reduces the oxidative burden and prevents cellular damage. In the presence of ROS, further stimulated through Fenton reactions of Cu^{2+}/H_2O_2, PrP:Cu^{2+} condensates transition into a gel-like state (less molecular mobility inside condensates) that inhibits functional Cu^{2+} sequestering by PrP. Moreover, ROS trigger PrP unfolding (exposure of hydrophobic surfaces), drive β-cleavage that produces aggregation-prone C-terminal PrP fragments, and enhance dityrosine cross-linking, altogether converting PrP into amyloid-like aggregates. In summary, PrP controls copper homeostasis and prevents ROS generation through phase separation, but abnormally high or prolonged ROS can result in aberrant PrP condensation and pathological aggregation. Scale bars are indicated inside images, and zoom-ins correspond to 2 μm.

Molecular features of PrP:Cu^{2+} phase separation

We showed that PrP forms liquid-like condensates that incorporate and accumulate Cu^{2+}, and this phase separation is mostly driven by electrostatic interactions, as 1,6-HD had a minor effect in disrupting condensation. PrP:Cu^{2+} phase separation was reduced upon slowly heating showing a minor participation of hydrophobic contacts, since protein dehydration caused by increasing temperature would enhance hydrophobic interactions. Furthermore, PrP:Cu^{2+} phase separation was enhanced at low temperatures pointing toward a lower critical solution temperature behavior characteristic of coacervation, whereby ionic interactions drive the intra/intermolecular labile cross-links involved in phase separation. PrP:Cu^{2+} condensates incubated with PrP seeds (produced with guanidinium/urea) do not show aggregation. Cu^{2+} is known to induce compactness and stability of PrP (*19*, *50*), which is in line with our results on PrP:Cu^{2+} condensates suppressing aggregation. Because recombinant PrPY145Stop (*47*), $PrP^{90–231}$ (*29*), and PrP with Hofmeister salt ($Na_2S_2O_3$) (*66*) formed hydrophobically driven condensates that undergo a liquid-to-solid transition, it is tempting to speculate that electrostatically driven PrP LLPS would be more functional. Reducing Cu^{2+} binding by EDTA or low pH reversed PrP LLPS, and Cu^{2+} prevented PrP aggregation, suggesting that PrP:Cu^{2+} LLPS and aggregation can occur independently, similarly to what has been suggested for Tau (*69*), or even that PrP:Cu^{2+} condensates might suppress aggregation as shown for α-synuclein (*70*). The octarepeats region in PrP is conserved across mammalian and avian species (*71*), indicating that Cu^{2+}-driven PrP LLPS may play a crucial role for cellular copper homeostasis.

Functional features of PrP:Cu^{2+} phase separation

In cells overexpressing PrP^C, Cu^{2+} induced large plasma membrane–bound PrP^C clusters that showed characteristics of liquid-like condensates (i.e., reduced molecular diffusion, fission, and fusion). Absorption of Cu^{2+} in cell surface PrP^C condensates at a 4:1 (Cu^{2+}:PrP) stoichiometry, similar to our in vitro observations, would provide an effective Cu^{2+} buffering system that counteracts metal ion toxicity, before redox-active copper would enter the cytosol. In normal conditions, PrP^C is endocytosed from the cell

surface with participation of clathrin-coated pits, caveolae, and rafts [reviewed in (*30*)]. In addition, PrP^C internalization is stimulated when neuronal cells are exposed to Cu^{2+} (*72*). However, the mechanism by which Cu^{2+} induces PrP^C internalization remains unknown as pointed out in many studies [reviewed in (*30*)]. Lysosomal storage of Cu^{2+}, and its redistribution to cellular compartments and metalloproteins that quench Cu^{2+} redox activity (*73*), could be facilitated through internalization of plasma membrane PrP^C:Cu^{2+} condensates by the endolysosomal pathway (*74*). In this case, we could expect release of Cu^{2+} in the acidic environment inside lysosomes (in vitro: no LLPS and no Cu^{2+} binding at pH of ~5), enabling lysosomal Cu^{2+} storage and/or mobilization together with the recycling of PrP^C back to the plasma membrane, to sequester more Cu^{2+} through condensation. Previous works suggested that PrP^C may act as copper buffer protecting cells from oxidative burden through an unknown mechanism, for example, during neuronal depolarization (*18*).

Our data deliver a LLPS-based cellular mechanism for these observations, in which PrP^C condensates sequester copper ions and prevent oxidative burden. Notably, PrP LLPS was also triggered by other metal ions in vitro (fig. S9), suggesting that membrane standing PrP^C condensates could provide a similar mechanism for other metal ions as well. Dysregulation of PrP:metal ion condensation could result in metal dyshomeostasis, as observed in early onset prion disease (*13*). PrP^C:Cu^{2+} condensates formed preferentially at cell-cell junctions, where PrP:Cu^{2+} condensation could also be involved in copper exchange between cells. PrP was reported to interact with proteins in adherens junctions and desmosomal junctions (*75*, *76*), and we recently suggested that the multivalency of these interactions could result in LLPS at cell-cell contacts (*31*).

Pathological features of PrP:Cu^{2+} phase separation

Extended Cu^{2+} incubation led to amyloid-like PrP^C aggregation on the cell surface, which is in line with the proposed pathological PrP^C to PrP^{Sc} conversion at the plasma membrane in prion diseases (*2*). From our in vitro data, we would assign this observation to the presence of ROS in the culture medium. ROS formation, triggered by Cu^{2+}-catalyzed Fenton reactions, resulted in (i) PrP β-cleavage, releasing the LLPS-driving N-terminal domain of PrP (*77*) and producing the aggregation-prone C-terminal fragment in minutes; (ii) triggered dityrosine formation; and (iii) induced liquid-to-solid transition of PrP condensates and the formation of amyloid-like PrP aggregates. In contrast, in non-oxidizing conditions (no H_2O_2), Cu^{2+} prevented PrP aggregation, supporting earlier findings that PrP:Cu^{2+} aggregates do not have amyloid content (*65*, *78*). Together, our data provide mechanistic insights into Cu^{2+}–driven PrP condensation as a way of cellular copper ion buffering and reveals the effects by which ROS triggers PrP aggregation in the presence of copper (Fig. 5D).

MATERIALS AND METHODS

Recombinant protein production

The pET-41 containing the coding region for mature full-length mouse PrP (residues 23 to 231) was transformed into competent *Escherichia coli* BL21 cells. The His-Tag of pET-41 was removed during cloning of PrP cDNA into NdeI and Hind III sites (*79*); hence, PrP was natively expressed without any tag. Protein expression was induced at 37°C for 16 to 18 hours in LB medium by addition of 0.5 mM isopropyl thio-β-D-galactoside, followed by PrP purification as previously described (*80*). Briefly, purification was achieved using Ni^{2+} affinity denaturing chromatography—taking advantage of the intrinsic ability of PrP octarepeat region (59-PHGGGWGQPHGGSWGQPHGGSWGQPHGGGWGQG-90, mouse protein residue numbering) to coordinate divalent transition metal ions, being a natural affinity tag—followed by in-column refolding and dialysis against ultrapure water. All chromatography steps were performed in an ÄKTA prime liquid chromatography system (GE Healthcare). Aliquots of PrP were kept at −20°C for up to 6 months.

Alexa Fluor 647 labeling of PrP

Purified PrP (150 μM; 0.5 ml) in 0.1 mM sodium bicarbonate (pH 8) and 1 M NaCl was incubated with 100 μg of succinimidyl ester of Alexa Fluor 647 (Thermo Fisher Scientific, A20006) in the dark for 1 hour at 25°C with gentle shaking. Uncoupled fluorophores were removed by chromatography in a HiTrap desalting column (Cytiva) equilibrated in 10 mM sodium phosphate (pH 5.8). The degree of labeling was calculated using dye absorbance at 650 nm and a molar extinction coefficient of 239,000 cm^{-1} M^{-1}. We obtained a PrP (2 μM; 3 ml) solution with a labeling yield of 1.2 mol of Alexa Fluor 647 per mol of PrP. The low protein yield is due to PrP precipitation and aggregation at high pH.

Sample preparation for LLPS assays

Samples of 25 μM PrP were immediately suspended in 0.22-μm filter-sterilized PhysB (Table 1). Subsequently, samples were incubated with 25 to 600 μM $CuCl_2$ and/or 10 mM H_2O_2, a known oxidizing condition for PrP, as reported in (*81*, *82*). For PhysB preparation, $CaCl_2$ was the first to be dissolved, whereas Hepes or K_2HPO_4/KH_2PO_4 was the last one added, to prevent $Ca_3(PO_4)_2$ precipitation (in case of K_2HPO_4/KH_2PO_4), followed by addition of PEG4K and pH adjustment with KOH. The buffers were prepared two times concentrated and kept at 4°C for 1 month. In the case of turbidity measurements, the concentration of PrP in samples was 10 μM in the presence or not of 2.5 to 120 μM $CuCl_2$ and/or 10 mM H_2O_2.

In vitro liquid-liquid phase separation studies by microscopy and turbidity

Ninety-six–well plates (flat-bottom, Sarstedt Inc. #82.1581) were coated with 0.5% (w/v) bovine serum albumin (Sigma-Aldrich, A2153) in 1× phosphate-buffered saline (PBS) for 1 hour in a see-saw rocker followed by 2× rinsing with ultrapure water. This step was carried out to provide a hydrophilic surface to the polystyrene plates. Protein solutions were immediately prepared in specified buffers as indicated in figure legends, and 50 μl (imaging) or 80 μl (turbidity) of solutions were added to each well followed by a 30-min incubation at room temperature. Imaging was carried out immediately after reactant addition (specified transition metals or $CuCl_2$ and/or H_2O_2) or at specified times in the figures. Samples described above were imaged in an inverted phase contrast microscope (EVOS FL Cell Imaging System, Thermo Fisher Scientific) with a 40× apochromat objective. For Zincon staining, phase-separated samples were deposited onto poli-D-lysine–coated glasses and incubated for 30 min, followed by the addition of a 0.4 mM Zincon solution [stock dissolved in 15 mM tris-HCl (pH 7.4)] and mount on coverslips sealed by nail polish. Turbidity (detected as

absorbance at 350 nm) assays were performed in a Synergy H1 spectrophotometer (BioTek Instruments) at 28°C.

Spectrophotometric determination of Cu^{2+} in the dense phase

A solution of PrP at 25 μM in 50 mM Hepes (pH 7.4), 125 mM NaCl, 150 μM $CaCl_2$, 5 mM $MgCl_2$, and 6% (w/v) PEG4K was incubated with 8× molar excess of $CuCl_2$ (200 μM). Upon addition of $CuCl_2$, phase separation was triggered, followed by sample equilibration for 1 hour in an ice bath at 0°C. To spin down the droplets, the sample was centrifuged at 100*g* for 30 min in a temperature-equilibrated centrifuge at 4°C. A blue pellet (i.e., dense phase) was formed in the bottom, and all supernatant (i.e., light phase) was removed to another tube. The pellet was weighted (0.0010 g) and solubilized in 4 μl of the light phase with addition of urea and nitric acid to a final concentration of 4 M and 2.4%, respectively, totalizing 20 μl of the pellet-containing solution. For colorimetric quantification of Cu^{2+}, we used a previously published protocol (*43*) in which samples are prepared in borate buffer containing 8 M urea (to release Cu^{2+} from protein).

Fluorescence recovery after photobleaching

In vitro FRAP experiments were performed in a confocal microscope (LSM 710, Zeiss) using a 100× oil immersion objective and 3× digital zoom. Solutions of unlabeled PrP spiked with 0.1% PrP–Alexa Fluor 647 were imaged (excitation wavelength at 633 nm; emission 638 to 755 nm) in a confocal dish (SPL Life Sciences, 200350). Bleaching was performed with a 405-nm laser (100% intensity, 1000 iterations; ~14 s total time), and started after 10 scans (scan rate, 390 ms) in circular ROIs (0.8 to 1.0 μm in diameter), followed by recovery monitoring for 50 to 90 s. In cellulo FRAP experiments using HEK293 cells (transfected with PrP^{C}-YFP-GPI or YFP-GPI) were performed in a spinning disk confocal microscope (Eclipse-Ti CSU-X, Nikon) equipped with an incubator for live cell imaging (37°C; 5% CO_2) using a 60× oil immersion objective. After five frames (scan rate, 200 ms), bleaching was set to two loops with a 10% 488-nm laser, and the recovery was monitored for 120 s. In all cases, unbleached and backgrounds ROIs of same size (area: 4.6 μm^2) were acquired simultaneously. Data were background-subtracted and normalized to the reference ROI to account for photofading during acquisition.

Immunofluorescence with anti-GRP78/BiP and LysoTracker staining

Fixed cells (4% paraformaldehyde) were Triton X-100–permeabilized cells followed by incubation with anti-GRP78/BIP (1:200; Abcam ab21685) in blocking solution [3% normal goat serum in PBS (pH 7.4)]. Subsequently, the secondary antibody (1:1000; goat anti-rabbit Alexa Fluor 647; Invitrogen) was added in blocking solution followed by Hoescht 33442 staining [1:500 in PBS (pH 7.4)]. LysoTracker Red DND-99 (Invitrogen) at 50 nM in Opti-MEM was incubated with live cells for 30 min (37°C, 5% CO_2). Subsequently, cells were washed two times and fixed with 4% paraformaldehyde.

BioTracker, AmyTracker, and Nile Red live cell staining

BioTracker 655 (Merck) was incubated at 1:500 molar ratio in Opti-MEM for 30 min (37°C, 5% CO_2) followed by two times washing and fresh medium addition. AmyTracker 680 (Ebba Biotech) labeling of live cells was performed with 1:1000 of the dye in Opti-MEM for 30 min (37°C, 5% CO_2) followed by replacing with fresh medium containing 300 μM $CuCl_2$ or not. In the case of Nile Red staining (0.1 μg/ml; Sigma-Aldrich), incubation was carried out in imaging solution [20 mM Hepes (pH 7.4), 140 mM NaCl, 2.5 mM KCl, 1.8 mM $CaCl_2$, 1.0 mM $MgCl_2$, and 20 mM D-glucose] for 30 min followed by replacing with fresh medium containing 300 μM $CuCl_2$ or not.

Transmission electron microscopy

Micrographs of PrP in the absence or presence of $CuCl_2$, H_2O_2, or both were acquired on a Hitachi HT7800 electron microscope operating at 100 kV. Grids were prepared by spotting 5 μl of samples on formvar/carbon-coated grid followed by contrasting with 2.0% uranyl acetate solution.

Turbidity as a function of temperature

Absorbance readings at 350 nm were carried out in a V-730 UV-VIS spectrophotometer (Jasco Corporation) equipped with a Koolance Cooling System EX2-755 using the Temperature Interval Scan Measurement tool. Sixty microliters of samples in 3-mm quartz cuvettes with corresponding micro cell jackets were previously equilibrated at the starting temperature for 30 min before measurements. A temperature gradient from 38° to 14°C and the return to the start temperature were run with a rate of 0.5°C/min and incubated for 30 s before each read.

Dynamic light scattering

Reads (10 accumulations each) were collected in a DynaPro NanoStar equipment (Wyatt Technology, CA, USA) with a GaAs laser at λ = 658 nm and intensity from 100 mW. Samples were immediately prepared in PhysB pH 7.2. The hydrodynamic radius of PEG4K in buffer solutions (without protein) was monitored and showed monodispersity, with particles varying from 0.7 to 0.9 nm and in all reads corresponded to 100% mass. DLS data were corrected with buffer properties, i.e., PhysB refraction index and viscosity at specified temperatures. The PhysB refraction index at 25°C (1.342) was measured using an Abbe refractometer. This buffer contains 6% (w/v) PEG4K; thus, to determine its viscosity (η), we retrieved the viscosity data of PEG4K aqueous solutions at 25°C determined by (*83*). From the linear regression, we obtained the viscosity of the PhysB (1.982×10^3 poiseuille).

Cell culture, transfection, and cell viability analysis

HEK293 cells were cultured in RPMI 1640 medium (Sigma-Aldrich) supplemented with 10% (v/v) FBS and 1% antibiotics penicillin/streptomycin (Gibco) at 37°C in 5% (v/v) CO_2 atmosphere. For cell transfection, cells were plated in 24-well plates [(SARSTEDT), for viability assay] and μ-Slide 8-well confocal dishes [(Ibidi), for imaging and FRAP] and transfected after 24 hours with Lipofectamine 2000 (Thermo Fisher Scientific) using 400 ng to 1 μg of specified plasmids [YFP-GPI (*84*), PrP^{C}-YFP-GPI, or GFP] in Opti-MEM (Thermo Fisher Scientific). Following 48 hours posttransfection, cells were treated with 10 to 1000 μM di-hydrated $CuCl_2$ (Sigma-Aldrich) for 1 hour. After treatment, cells were detached with trypsin solution (Nova Biotecnologia) and quantified using Trypan blue solution [0.2% (w/v) in PBS] in a hemocytometer. For FRAP, transfected cells had medium exchanged to fresh Opti-MEM 1 hour before addition of 300 μM $CuCl_2$. After

30 min to 1 hour of incubation with $CuCl_2$ or not, FRAP experiments were performed.

Immunoblotting

Whole-cell extracts were obtained 24 hours posttransfection using mild radioimmunoprecipitation assay buffer [50 mM tris-HCl (pH 7.4), 150 mM NaCl,1 mM EDTA, and NP-40 1% (v/v)] supplemented with protease inhibitor cocktail 1% (v/v) (Sigma-Adlrich) and quantified by Bradford assay. Protein extracts (50 μg per lane) were resolved in 15% SDS-PAGE followed by immunoblotting using anti-GFP (AB3080P, Merck), anti-PrP^C monoclonal antibody (anti-CD320, clone 6D11; BioLegend, 808001), and anti–β-actin (Invitrogen, MA5-15739) as loading control. Horseradish peroxidase–linked conjugated secondary antibodies (Invitrogen) were developed with SuperSignal West Pico Chemiluminescent Substrate (Thermo Fisher Scientific, 34077) using a Chemidoc scanner (Bio-Rad).

X-ray photon correlation spectroscopy

XPCS experiments were performed at the CATERETÊ beamline (Brazilian Center for Research in Energy and Materials) at a photon energy of 10 keV (1% bandwidth). Data were collected using a PiMega540D detector in small-angle x-ray scattering (SAXS) geometry at a sample detector distance of 27.6 m allowing measurement of low scattering vector (q) values ($q = 4\pi\sin\theta/\lambda$, being 2θ the angle between the incident and scattered beam). Samples of PrP (25 μM) with or without $CuCl_2$ (200 μM) and/or H_2O_2 (10 mM) were prepared immediately before measurements, and condensate formation was monitored by differential interference contrast (DIC) microscopy in situ (Leica LMD 7). Each sample was filled into 1.5-mm-diameter quartz capillaries. To mitigate radiation damage, samples were measured with sapphire attenuator, and the total time was considered as time with no visible change in the SAXS patterns. The XPCS experiments have been performed below this threshold dose value. All samples were analyzed in PhysB pH 7.2 at 25°C. The autocorrelation functions can be expressed by the Kohlrausch-Williams-Watts (KWW) model (Eq. 1) containing information about the time scales and type of motion in protein condensates.

$$g^2(q,t) = 1 + \beta\exp[-2(\Gamma\tau)^{\gamma}] \quad (1)$$

where β is the contrast factor, Γ is the relaxation rate, τ is the delay time, q is the scattering vector, and γ is the KWW exponent. The dynamics is quantified by the relaxation rate (fig. S11D) and characterized by the KWW exponent γ (Fig. 3G), where $\gamma = 1$ represents a single exponential decay corresponding to Brownian diffusion. When $\gamma > 1$, the relaxation process is faster than exponential (superdiffusive), often seen in disordered soft solids like gels, and $\gamma < 1$ is indicative of relaxation slower than exponential decay (subdiffusive), commonly observed in systems with several competing relaxation mechanisms, such as liquids near the glass transition temperature.

Steady-state fluorescence and anisotropy

Intrinsic tryptophan fluorescence was recorded with excitation set at 295 nm and emission verified from 310 to 400 nm with 5 μM PrP and varying $CuCl_2$ concentration (from 5 to 40 μM). Tryptophan fluorescence as a function of temperature was collected upon slowly heating in steps of 1°C from 25° to 80°C. The center of spectral mass (CM) in nanometers was calculated via the equation: $CM = \Sigma\, \nu i Fi/\Sigma\, Fi$, where νi is the wavelength and Fi is the fluorescence intensity at each wavelength. Dityrosine fluorescence was recorded with excitation at 325 nm and emission from 350 to 500 nm. SYPRO orange fluorescence (stock 5000× in DMSO; working concentration 50×) was recorded with excitation at 495 nm and emission from 535 to 665 nm. Both dityrosine and SYPRO fluorescence were monitored for 25 μM PrP aggregated samples. The probe 1,8-ANS (at 30 μM) was added to aggregated or soluble 20 μM PrP, and its fluorescence emission was collected from 400 to 600 nm upon excitation at 360 nm. Tryptophan anisotropy (excitation, 280 nm; emission, 353 nm) of 25 μM PrP was acquired upon $CuCl_2$ titration at 25°C in a Cary Eclipse Fluorescence Spectrophotometer (Agilent) with slits of 5 nm (excitation) and 10 nm (emission). ThT assays were run for 72 hours at 42°C in a ClarioStar plate reader (BMG Labtech, Germany) using a 96-well black plate (SARSTEDT No. 82.1581.220) containing Teflon polyballs [$^1/_8$-in (0.3175 cm) diameter]. Plates were sealed with an optically clear transparent film (Axygen, #UC-500). Fluorescence emission was collected from the top (excitation wavelength: 448 nm; emission wavelength: 482 nm), and readings were collected after double-orbital shaking (600 rpm; 30 s) every 5 min (20 flashes per reading). Each well had 120 μl of 25 μM PrP solutions with 0.1% seed in the presence of $CuCl_2$ (200 μM) or not in PhysB pH 7.2 containing 30 μM ThT and 3 mM NaN_3. All assays were performed in PhysB at 25°C in a FP-8250 Spectrofluorometer (Jasco) equipped with a thermal control unit (with a Koolance Cooling System EX2−755), unless otherwise stated.

Circular dichroism

CD data were collected on a Chirascan Circular Dichroism Spectrometer (Applied Photophysics) using 2-mm-quartz cell at 25°C. Spectra were recorded over 190 to 260 nm wavelength range at 1-nm intervals at a speed of 0.5 s per point and reported as the average of three measurements. All spectra were subtracted from the corresponding background buffer spectrum and smoothed by a Savitzky-Golay filter with a window size of 4. Data were expressed as molar ellipticity [θ] or ellipticity (θ) in millidegrees (mdeg). The mean amino acid residue weight (MRW) of PrP is 100. Molar residue ellipticity [θ] was calculated with the following equation: $[\theta] = (MRW \times \theta\lambda)/(c \times l \times 10)$ where θλ is the observed ellipticity (millidegrees), c is the protein concentration (grams per milliliter), and l is the cell pathlength (0.2 cm).

Image, data, and statistical analysis

Phase contrast, DIC, and fluorescence representative micrographs from at least three independent experiments had their brightness/contrast corrected by histogram stretching using Fiji (*85*). Line profile, image quantification, and in-cell FRAP were analyzed using Fiji. All data and statistical tests (specified in the figure legends) were plotted and analyzed using Prism 8.1.1 (GraphPad Software).

Supplementary Materials

This PDF file includes:

Figs. S1 to S15

Legends for movies S1 to S4

Other Supplementary Material for this manuscript includes the following:
Movies S1 to S4

REFERENCES AND NOTES

1. S. B. Prusiner, Prions. *Proc. Natl. Acad. Sci.* **95**, 13363–13383 (1998).
2. B. Caughey, G. S. Baron, B. Chesebro, M. Jeffrey, Getting a grip on prions: Oligomers, amyloids, and pathological membrane interactions. *Annu. Rev. Biochem.* **78**, 177–204 (2009).
3. S. J. Kim, R. S. Hegde, Cotranslational partitioning of nascent prion protein into multiple populations at the translocation channel. *Mol. Biol. Cell* **13**, 3775–3786 (2002).
4. C. J. Johnson, P. U. P. A. Gilbert, M. Abrecht, K. L. Baldwin, R. E. Russell, J. A. Pedersen, J. M. Aiken, D. McKenzie, Low copper and high manganese levels in prion protein plaques. *Viruses* **5**, 654–662 (2013).
5. O. Milhavet, H. E. M. McMahon, W. Rachidi, N. Nishida, S. Katamine, A. Mangé, M. Arlotto, D. Casanova, J. Riondel, A. Favier, S. Lehmann, Prion infection impairs the cellular response to oxidative stress. *Proc. Natl. Acad. Sci. U.S.A.* **97**, 13937–13942 (2000).
6. M. J. Pushie, I. J. Pickering, G. R. Martin, S. Tsutsui, F. R. Jirik, G. N. George, Prion protein expression level alters regional copper, iron and zinc content in the mouse brain. *Metallomics* **3**, 206–214 (2011).
7. T. Nishimura, A. Sakudo, I. Nakamura, D. C. Lee, Y. Taniuchi, K. Saeki, Y. Matsumoto, M. Ogawa, S. Sakaguchi, S. Itohara, T. Onodera, Cellular prion protein regulates intracellular hydrogen peroxide level and prevents copper-induced apoptosis. *Biochem. Biophys. Res. Commun.* **323**, 218–222 (2004).
8. D. R. Brown, W. J. Schulz-Schaeffer, B. Schmidt, H. A. Kretzschmar, Prion protein-deficient cells show altered response to oxidative stress due to decreased SOD-1 activity. *Exp. Neurol.* **146**, 104–112 (1997).
9. G. L. Millhauser, Copper and the prion protein: Methods, structures, function, and disease. *Annu. Rev. Phys.Chem.* **58**, 299–320 (2007).
10. D. R. Brown, K. Qin, J. W. Herms, A. Madlung, J. Manson, R. Strome, P. E. Fraser, T. Kruck, A. von Bohlen, W. Schulz-Schaeffer, A. Giese, D. Westaway, H. Kretzschmar, The cellular prion protein binds copper in vivo. *Nature* **390**, 684–687 (1997).
11. E. D. Walter, M. Chattopadhyay, G. L. Millhauser, The affinity of copper binding to the prion protein octarepeat domain: Evidence for negative cooperativity. *Biochemistry* **45**, 13083–13092 (2006).
12. M. Hodak, R. Chisnell, W. Lu, J. Bernholc, Functional implications of multistage copper binding to the prion protein. *Proc. Natl. Acad. Sci. U.S.A.* **106**, 11576–11581 (2009).
13. D. R. Brown, "Metals and Prions: Twenty Years of Mining the Awe" in Biometals in Neurodegenerative Diseases: Mechanisms and Therapeutics (2017), pp. 95–115.
14. N. T. Watt, D. R. Taylor, T. L. Kerrigan, H. H. Griffiths, J. V. Rushworth, I. J. Whitehouse, N. M. Hooper, Prion protein facilitates uptake of zinc into neuronal cells. *Nat. Commun.* **3**, 1134 (2012).
15. T. Miura, S. Sasaki, A. Toyama, H. Takeuchi, Copper reduction by the octapeptide repeat region of prion protein: PH dependence and implications in cellular copper uptake. *Biochemistry* **44**, 8712–8720 (2005).
16. D. R. Brown, C. Clive, S. J. Haswell, Antioxidant activity related to copper binding of native prion protein. *J. Neurochem.* **76**, 69–76 (2001).
17. G. L. Millhauser, Copper binding in the prion protein. *Acc. Chem. Res.* **37**, 79–85 (2004).
18. G. Salzano, G. Giachin, G. Legname, Structural consequences of copper binding to the prion protein. *Cell* **8**, 770 (2019).
19. K. M. Schilling, L. Tao, B. Wu, J. T. M. Kiblen, N. C. Ubilla-Rodriguez, M. J. Pushie, R. D. Britt, G. P. Roseman, D. A. Harris, G. L. Millhauser, Both N-terminal and C-terminal histidine residues of the prion protein are essential for copper coordination and neuroprotective self-regulation. *J. Mol. Biol.* **432**, 4408–4425 (2020).
20. Y. Watanabe, W. Hiraoka, M. Igarashi, K. Ito, Y. Shimoyama, M. Horiuchi, T. Yamamori, H. Yasui, M. Kuwabara, F. Inagaki, O. Inanami, A novel copper(II) coordination at His^{186} in full-length murine prion protein. *Biochem. Biophys. Res. Commun.* **394**, 522–528 (2010).
21. E. W. Martin, A. S. Holehouse, I. Peran, M. Farag, J. J. Incicco, A. Bremer, C. R. Grace, A. Soranno, R. V. Pappu, T. Mittag, Valence and patterning of aromatic residues determine the phase behavior of prion-like domains. *Science* **367**, 694–699 (2020).
22. M. P. Hughes, M. R. Sawaya, D. R. Boyer, L. Goldschmidt, J. A. Rodriguez, D. Cascio, L. Chong, T. Gonen, D. S. Eisenberg, Atomic structures of low-complexity protein segments reveal kinked β sheets that assemble networks. *Science* **359**, 698–701 (2018).
23. M. P. Hughes, L. Goldschmidt, D. S. Eisenberg, Prevalence and species distribution of the low-complexity, amyloid-like, reversible, kinked segment structural motif in amyloid-like fibrils. *J. Biol. Chem.* **297**, 101194 (2021).
24. S. Boeynaems, S. Alberti, N. L. Fawzi, T. Mittag, M. Polymenidou, F. Rousseau, J. Schymkowitz, J. Shorter, B. Wolozin, L. Van Den Bosch, P. Tompa, M. Fuxreiter, Protein phase separation: A new phase in cell biology. *Trends Cell Biol.* **28**, 420–435 (2018).
25. S. Alberti, A. A. Hyman, Biomolecular condensates at the nexus of cellular stress, protein aggregation disease and ageing. *Nat. Rev. Mol. Cell Biol.* **22**, 196–213 (2021).
26. S. Elbaum-Garfinkle, Matter over mind: Liquid phase separation and neurodegeneration. *J. Biol. Chem.* **294**, 7160–7168 (2019).
27. S. Wegmann, B. Eftekharzadeh, K. Tepper, K. M. Zoltowska, R. E. Bennett, S. Dujardin, P. R. Laskowski, D. MacKenzie, T. Kamath, C. Commins, C. Vanderburg, A. D. Roe, Z. Fan, A. M. Molliex, A. Hernandez-Vega, D. Muller, A. A. Hyman, E. Mandelkow, J. P. Taylor, B. T. Hyman, Tau protein liquid–liquid phase separation can initiate tau aggregation. *EMBO J.* **37**, e98049 (2018).
28. M. A. Kostylev, M. D. Tuttle, S. Lee, L. E. Klein, H. Takahashi, T. O. Cox, E. C. Gunther, K. W. Zilm, S. M. Strittmatter, Liquid and hydrogel phases of PrP^C linked to conformation shifts and triggered by Alzheimer's amyloid-β oligomers. *Mol. Cell* **72**, 426–443.e12 (2018).
29. C. O. Matos, Y. M. Passos, M. J. Amaral, B. Macedo, M. H. Tempone, O. C. L. Bezerra, M. O. Moraes, M. S. Almeida, G. Weber, S. Missailidis, J. L. Silva, V. N. Uversky, A. S. Pinheiro, Y. Cordeiro, Liquid-liquid phase separation and fibrillation of the prion protein modulated by a high-affinity DNA aptamer. *FASEB J.* **34**, 365–385 (2020).
30. V. Campana, D. Sarnataro, C. Zurzolo, The highways and byways of prion protein trafficking. *Trends Cell Biol.* **15**, 102–111 (2005).
31. M. J. do Amaral, M. H. O. Freire, M. S. Almeida, A. S. Pinheiro, Y. Cordeiro, Phase separation of the mammalian prion protein: Physiological and pathological perspectives. *J. Neurochem.* **166**, 58–75 (2023).
32. A. Agarwal, L. Arora, S. K. Rai, A. Avni, S. Mukhopadhyay, Spatiotemporal modulations in heterotypic condensates of prion and α-synuclein control phase transitions and amyloid conversion. *Nat. Commun.* **13**, 1154 (2022).
33. L. Varela-Nallar, E. M. Toledo, L. F. Larrondo, A. L. B. Cabral, V. R. Martins, N. C. Inestrosa, Induction of cellular prion protein gene expression by copper in neurons. *Am. J. Physiol. Cell Physiol.* **290**, C271–C281 (2006).
34. O. Beutel, R. Maraspini, K. Pombo-García, C. Martin-Lemaitre, A. Honigmann, Phase separation of zonula occludens proteins drives formation of tight junctions. *Cell* **179**, 923–936.e11 (2019).
35. S. E. Encalada, L. Szpankowski, C. H. Xia, L. S. B. Goldstein, Stable kinesin and dynein assemblies drive the axonal transport of mammalian prion protein vesicles. *Cell* **144**, 551–565 (2011).
36. L. Ivanova, S. Barmada, T. Kummer, D. A. Harris, Mutant prion proteins are partially retained in the endoplasmic reticulum. *J. Biol. Chem.* **276**, 42409–42421 (2001).
37. M. Vendruscolo, M. Fuxreiter, Sequence determinants of the aggregation of proteins within condensates generated by liquid-liquid phase separation. *J. Mol. Biol.* **434**, 167201 (2022).
38. B. Bolognesi, N. L. Gotor, R. Dhar, D. Cirillo, M. Baldrighi, G. G. Tartaglia, B. Lehner, A concentration-dependent liquid phase separation can cause toxicity upon increased protein expression. *Cell Rep.* **16**, 222–231 (2016).
39. E. A. Paiz, J. H. Allen, J. J. Correia, N. C. Fitzkee, L. E. Hough, S. T. Whitten, Beta turn propensity and a model polymer scaling exponent identify intrinsically disordered phase-separating proteins. *J. Biol. Chem.* **297**, 101343 (2021).
40. R. M. C. Vernon, P. A. Chong, B. Tsang, T. H. Kim, A. Bah, P. Farber, H. Lin, J. D. Forman-Kay, Pi-Pi contacts are an overlooked protein feature relevant to phase separation. *eLife* **7**, e31486 (2018).
41. D. J. Stevens, E. D. Walter, A. Rodríguez, D. Draper, P. Davies, D. R. Brown, G. L. Millhauser, Early onset prion disease from octarepeat expansion correlates with copper binding properties. *PLOS Pathog.* **5**, e1000390 (2009).
42. P. Davies, F. Marken, S. Salter, D. R. Brown, Thermodynamic and voltammetric characterization of the metal binding to the prion protein: Insights into pH dependence and redox chemistry. *Biochemistry* **48**, 2610–2619 (2009).
43. C. E. Säbel, J. M. Neureuther, S. Siemann, A spectrophotometric method for the determination of zinc, copper, and cobalt ions in metalloproteins using Zincon. *Anal. Biochem.* **397**, 218–226 (2010).
44. C. Q. Xiao, Q. Huang, Y. Zhang, H. Q. Zhang, L. Lai, Binding thermodynamics of divalent metal ions to several biological buffers. *Thermochim. Acta* **691**, 178721 (2020).
45. J. H. Viles, F. E. Cohen, S. B. Prusiner, D. B. Goodin, P. E. Wright, H. J. Dyson, Copper binding to the prion protein: Structural implications of four identical cooperative binding sites. *Proc. Natl. Acad. Sci. U.S.A.* **96**, 2042–2047 (1999).
46. M. Sokołowska, W. Bal, Cu(II) complexation by "non-coordinating" *N*-2-hydroxyethylpiperazine-*N'*-2-ethanesulfonic acid (HEPES buffer). *J. Inorg. Biochem.* **99**, 1653–1660 (2005).
47. A. Agarwal, S. K. Rai, A. Avni, S. Mukhopadhyay, An intrinsically disordered pathological prion variant Y145Stop converts into self-seeding amyloids via liquid-liquid phase separation. *Proc. Natl. Acad. Sci. U.S.A.* **118**, e2100968118 (2021).

48. J. Hochmair, C. Exner, M. Franck, A. Dominguez-Baquero, L. Diez, H. Brognaro, M. L. Kraushar, T. Mielke, H. Radbruch, S. Kaniyappan, S. Falke, E. Mandelkow, C. Betzel, S. Wegmann, Molecular crowding and RNA synergize to promote phase separation, microtubule interaction, and seeding of Tau condensates. *EMBO J.* **41**, e108882 (2022).
49. A. P. Garnett, J. H. Viles, Copper binding to the octarepeats of the prion protein. affinity, specificity, folding, and cooperativity: Insights from circular dichroism. *J. Biol. Chem.* **278**, 6795–6802 (2003).
50. A. K. Thakur, A. K. Srivastava, V. Srinivas, K. V. R. Chary, C. M. Rao, Copper alters aggregation behavior of prion protein and induces novel interactions between its N- and C-terminal regions. *J. Biol. Chem.* **286**, 38533–38545 (2011).
51. F. T. S. Chan, G. S. Kaminski Schierle, J. R. Kumita, C. W. Bertoncini, C. M. Dobson, C. F. Kaminski, Protein amyloids develop an intrinsic fluorescence signature during aggregation. *Analyst* **138**, 2156–2162 (2013).
52. H. Zhang, The glassiness of hardening protein droplets. *Science* **370**, 1271–1272 (2020).
53. L. Jawerth, E. Fischer-Friedrich, S. Saha, J. Wang, T. Franzmann, X. Zhang, J. Sachweh, M. Ruer, M. Ijavi, S. Saha, J. Mahamid, A. A. Hyman, F. Jülicher, Protein condensates as aging Maxwell fluids. *Science* **370**, 1317–1323 (2020).
54. A. Girelli, H. Rahmann, N. Begam, A. Ragulskaya, M. Reiser, S. Chandran, F. Westermeier, M. Sprung, F. Zhang, C. Gutt, F. Schreiber, Microscopic Dynamics of liquid-liquid phase separation and domain coarsening in a protein solution revealed by X-ray photon correlation spectroscopy. *Phys. Rev. Lett.* **126**, 138004 (2021).
55. M. Moron, A. Al-Masoodi, C. Lovato, M. Reiser, L. Randolph, G. Surmeier, J. Bolle, F. Westermeier, M. Sprung, R. Winter, M. Paulus, C. Gutt, Gelation dynamics upon pressure-induced liquid-liquid phase separation in a water-lysozyme solution. *J. Phys. Chem. B* **126**, 4160–4167 (2022).
56. L. Cipelletti, L. Ramos, S. Manley, E. Pitard, D. A. Weitz, E. E. Pashkovski, M. Johansson, Universal non-diffusive slow dynamics in aging soft matter. *Faraday Discuss.* **123**, 237–251 (2003).
57. N. C. Ferreira, L. M. Ascari, A. G. Hughson, G. R. Cavalheiro, C. F. Góes, P. N. Fernandes, J. R. Hollister, R. A. Da Conceição, D. S. Silva, A. M. T. Souza, M. L. C. Barbosa, F. A. Lara, R. A. P. Martins, B. Caughey, Y. Cordeiro, A promising antiprion trimethoxychalcone binds to the globular domain of the cellular prion protein and changes its cellular location. *Antimicrob. Agents Chemother.* **62**, e01441-17 (2018).
58. A. K. Mora, S. Nath, SYPRO Orange-a new gold standard amyloid probe. *J. Mater. Chem. B* **8**, 7894–7898 (2020).
59. M. B. Maina, G. Burra, Y. K. Al-Hilaly, K. Mengham, K. Fennell, L. C. Serpell, Metal- and UV-catalyzed oxidation results in trapped Amyloid-β intermediates revealing that self-assembly is required for Aβ-induced cytotoxicity. *iScience* **23**, 101537 (2020).
60. F. Hoyt, P. Alam, E. Artikis, C. L. Schwartz, A. G. Hughson, B. Race, C. Baune, G. J. Raymond, G. S. Baron, A. Kraus, B. Caughey, Cryo-EM of prion strains from the same genotype of host identifies conformational determinants. *PLOS Pathog.* **18**, e1010947 (2022).
61. H. E. M. McMahon, A. Mangé, N. Nishida, C. Créminon, D. Casanova, S. Lehmann, Cleavage of the amino terminus of the prion protein by reactive oxygen species. *J. Biol. Chem.* **276**, 2286–2291 (2001).
62. L. Linsenmeier, H. C. Altmeppen, S. Wetzel, B. Mohammadi, P. Saftig, M. Glatzel, Diverse functions of the prion protein – Does proteolytic processing hold the key? *Biochim. Biophys. Acta Mol. Cell Res.* **1864**, 2128–2137 (2017).
63. C. King, P. Sengupta, A. Y. Seo, J. Lippincott-Schwartz, ER membranes exhibit phase behavior at sites of organelle contact. *Proc. Natl. Acad. Sci. U.S.A.* **117**, 7225–7235 (2020).
64. M. E. Sitar, S. Aydin, U. Çakatay, Human serum albumin and its relation with oxidative stress. *Clin. Lab.* **59**, 945–952 (2013).
65. O. V. Bocharova, L. Breydo, V. V. Salnikov, I. V. Baskakov, Copper(II) inhibits in vitro conversion of prion protein into amyloid fibrils. *Biochemistry* **44**, 6776–6787 (2005).
66. H. Tange, D. Ishibashi, T. Nakagaki, Y. Taguchi, Y. O. Kamatari, H. Ozawa, N. Nishida, Liquid liquid phase separation of full-length prion protein initiates conformational conversion in vitro. *J. Biol. Chem.* **296**, 100367 (2021).
67. Y. M. Passos, M. J. do Amaral, N. C. Ferreira, B. Macedo, J. A. P. Chaves, V. E. de Oliveira, M. P. B. Gomes, J. L. Silva, Y. Cordeiro, The interplay between a GC-rich oligonucleotide and copper ions on prion protein conformational and phase transitions. *Int. J. Biol. Macromol.* **173**, 34–43 (2021).
68. J. Kamps, Y. H. Lin, R. Oliva, V. Bader, R. Winter, K. F. Winklhofer, J. Tatzelt, The N-terminal domain of the prion protein is required and sufficient for liquid-liquid phase separation: A crucial role of the Aβ-binding domain. *J. Biol. Chem.* **297**, 100860 (2021).
69. Y. Lin, Y. Fichou, Z. Zeng, N. Y. Hu, S. Han, Electrostatically driven complex coacervation and amyloid aggregation of tau are independent processes with overlapping conditions. *ACS Chem. Nerosci.* **11**, 615–627 (2020).
70. W. P. Lipiński, B. S. Visser, I. Robu, M. A. A. Fakhree, S. Lindhoud, M. M. A. E. Claessens, E. Spruijt, Biomolecular condensates can both accelerate and suppress aggregation of α-synuclein. *Sci. Adv.* **8**, eabq6495 (2022).
71. F. Wopfner, G. Weidenhöfer, R. Schneider, A. von Brunn, S. Gilch, T. F. Schwarz, T. Werner, H. M. Schätzl, Analysis of 27 mammalian and 9 avian PrPs reveals high conservation of flexible regions of the prion protein. *J. Mol. Biol.* **289**, 1163–1178 (1999).
72. P. C. Pauly, D. A. Harris, Copper stimulates endocytosis of the prion protein. *J. Biol. Chem.* **273**, 33107–33110 (1998).
73. E. V. Polishchuk, R. S. Polishchuk, The emerging role of lysosomes in copper homeostasis. *Metallomics* **8**, 853–862 (2016).
74. L.-P. Bergeron-Sandoval, S. Kumar, H. K. Heris, C. L. A. Chang, C. E. Cornell, S. L. Keller, P. François, A. G. Hendricks, A. J. Ehrlicher, R. V. Pappu, S. W. Michnick, Endocytic proteins with prion-like domains form viscoelastic condensates that enable membrane remodeling. *Proc. Natl. Acad. Sci.* **118**, e2113789118 (2021).
75. C. S. V. Petit, L. Besnier, E. Morel, M. Rousset, S. Thenet, Roles of the cellular prion protein in the regulation of cell-cell junctions and barrier function. *Tissue Barriers* **1**, e24377 (2013).
76. A. Kouadri, M. El Khatib, J. Cormenier, S. Chauvet, W. Zeinyeh, M. El Khoury, L. MacAri, P. Richaud, C. Coraux, I. Michaud-Soret, N. Alfaidy, M. Benharouga, Involvement of the prion protein in the protection of the human bronchial epithelial barrier against oxidative stress. *Antioxid. Redox Signal.* **31**, 59–74 (2019).
77. A. Mangé, F. Béranger, K. Peoc'h, T. Onodera, Y. Frobert, S. Lehmann, Alpha- and beta-cleavages of the amino-terminus of the cellular prion protein. *Biol. Cell* **96**, 125–132 (2004).
78. E. Quaglio, R. Chiesa, D. A. Harris, Copper converts the cellular prion protein into a protease-resistant species that is distinct from the scrapie isoform. *J. Biol. Chem.* **276**, 11432–11438 (2001).
79. R. Atarashi, R. A. Moore, V. L. Sim, A. G. Hughson, D. W. Dorward, H. A. Onwubiko, S. A. Priola, B. Caughey, Ultrasensitive detection of scrapie prion protein using seeded conversion of recombinant prion protein. *Nat. Methods* **4**, 645–650 (2007).
80. B. Macedo, R. Sant'Anna, S. Navarro, Y. Cordeiro, S. Ventura, Mammalian prion protein (PrP) forms conformationally different amyloid intracellular aggregates in bacteria. *Microb. Cell Fact.* **14**, 174 (2015).
81. N. D. Younan, R. C. Nadal, P. Davies, D. R. Brown, J. H. Viles, Methionine oxidation perturbs the structural core of the prion protein and suggests a generic misfolding pathway. *J. Biol. Chem.* **287**, 28263–28275 (2012).
82. J. R. Requena, D. Groth, G. Legname, E. R. Stadtman, S. B. Prusiner, R. L. Levine, Copper-catalyzed oxidation of the recombinant SHa(29-231) prion protein. *Proc. Natl. Acad. Sci. U.S.A.* **98**, 7170–7175 (2001).
83. S. Kiriňi, C. Klofutar, Viscosity of aqueous solutions of poly(ethylene glycol)s at 298.15 K. *Fluid Phase Equilib.* **155**, 311–325 (1999).
84. D. F. Legler, M.-A. Doucey, P. Schneider, L. Chapatte, F. C. Bender, C. Bron, Differential insertion of GPI-anchored GFPs into lipid rafts of live cells. *FASEB J.* **19**, 73–75 (2005).
85. J. Schindelin, I. Arganda-Carreras, E. Frise, V. Kaynig, M. Longair, T. Pietzsch, S. Preibisch, C. Rueden, S. Saalfeld, B. Schmid, J. Y. Tinevez, D. J. White, V. Hartenstein, K. Eliceiri, P. Tomancak, A. Cardona, Fiji: An open-source platform for biological-image analysis. *Nat. Methods* **9**, 676–682 (2012).
86. J. Kardos, I. Kovács, F. Hajós, M. Kálmán, M. Simonyi, Nerve endings from rat brain tissue release copper upon depolarization. A possible role in regulating neuronal excitability. *Neurosci. Lett.* **103**, 139–144 (1989).
87. J. Stöckel, J. Safar, A. C. Wallace, F. E. Cohen, S. B. Prusiner, Prion protein selectively binds copper(II) ions. *Biochemistry* **37**, 7185–7193 (1998).
88. L. Zecca, A. Stroppolo, A. Gatti, D. Tampellini, M. Toscani, M. Gallorini, G. Giaveri, P. Arosio, P. Santambrogio, R. G. Fariello, E. Karatekin, M. H. Kleinman, N. Turro, O. Hornykiewicz, F. A. Zucca, The role of iron and copper molecules in the neuronal vulnerability of locus coeruleus and substantia nigra during aging. *Proc. Natl. Acad. Sci. U.S.A.* **101**, 9843–9848 (2004).
89. A. Hopt, S. Korte, H. Fink, U. Panne, R. Niessner, R. Jahn, H. Kretzschmar, J. Herms, Methods for studying synaptosomal copper release. *J. Neurosci. Methods* **128**, 159–172 (2003).
90. J. Herms, T. Tings, S. Gall, A. Madlung, A. Giese, H. Siebert, O. Peter Schürmann, T. Windl, N. Brose, H. Kretzschmar, Evidence of presynaptic location and function of the prion protein. *J. Neurosci.* **19**, 8866–8875 (1999).
91. D. E. Knight, M. C. Scrutton, Gaining access to the cytosol: The technique and some applications of electropermeabilization. *Biochem. J.* **234**, 497–506 (1986).
92. M. J. B. Van Den Hoff, A. F. M. Moorman, W. H. Lamers, Electroporation in "intracellular" buffer increases cell survival. *Nucleic Acids Res.* **20**, 2902 (1992).
93. F. X. Theillet, A. Binolfi, T. Frembgen-Kesner, K. Hingorani, M. Sarkar, C. Kyne, C. Li, P. B. Crowley, L. Gierasch, G. J. Pielak, A. H. Elcock, A. Gershenson, P. Selenko, Physicochemical properties of cells and their effects on intrinsically disordered proteins (IDPs). *Chem. Rev.* **114**, 6661–6714 (2014).

Acknowledgments: We thank CENABIO (Universidade Federal do Rio de Janeiro, Brazil) and AMBIO (Charité Universitätsmedizin, Berlin) imaging facilities. We thank M. H. Lopes (Universidade de São Paulo, Brazil) for providing us with the PrP^{C}-YFP-GPI plasmid and D. Legler

(Universität Konstanz, Germany) for the YFP-GPI plasmid. We acknowledge F. Meneau (LNLS, Brazil) and P. Garcia (LNLS, Brazil) for the development of the XPCS package. We thank J. L. Silva (UFRJ, Brazil) for insightful discussions. We thank S. Hübschmann (DZNE-Berlin, Germany) and M. Heloisa Freire (UFRJ, Brazil) for help in cell culture. We thank T. Sisnande (UFRJ, Brazil) for help in imaging Zincon stained samples. Cell microscopy was performed in the AMBIO imaging core of the Charité Berlin. Figure 5D was created with BioRender. **Funding:** This work was supported by Coordenação de Aperfeiçoamento de Pessoal de Nível Superior–Brasil (CAPES) (Finance Code 001) (M.J.A.), Fundação de Amparo à Pesquisa do Estado do Rio de Janeiro (FAPERJ) grants 202.625/2019 and 200.562/2023 (Y.C.), Fundação de Amparo à Pesquisa do Estado do Rio de Janeiro (FAPERJ) grant 201.439/2021 (R.S.C.), Fundação de Amparo à Pesquisa do Estado do Rio de Janeiro (FAPERJ) grant 200.977/2022 (A.S.P.), Fundação de Amparo à Pesquisa do Estado do Rio de Janeiro (FAPERJ) (M.S.A.), Conselho Nacional de Desenvolvimento Científico e Tecnológico (CNPq) grant 307294/2018-8 (Y.C.), Conselho Nacional de Desenvolvimento Científico e Tecnológico (CNPq) grant 306710/2021-8 (A.S.P.), Conselho Nacional de Desenvolvimento Científico e Tecnológico (CNPq) (M.S.A.), Brazilian Synchrotron Light Laboratory (LNLS) of the Brazilian Ministry for Science, Technology, Innovations and Communications (MCTIC) (CATERETE-20220546) (Y.C.), CAPES-PrInt scholarship, grant number 88887.695190/2022-00 (M.J.A.), German Research Society (DFG), priority program SPP2191 (419138680) (S.W.), Helmholtz Association, Institutional funding (S.W.), and Hertie Foundation (P1200002) (S.W.). **Author contributions:** M.J.A. conceived and designed the study, wrote the original draft, and involved in all experiments and data analysis. A.R.P. and Y.C. performed the XPCS data collection and analysis. S.M. performed live-cell imaging and FRAP and helped with image analysis. T.S.L.S. and R.C.S. performed cell viability assay, Western blotting, and analysis. Y. C., S.W., M.S.A., A.S.P., and R.C.S. performed grant acquisition. Y.C., M.S.A., A.S.P., and S.W. supervised the study. Y.C., A.S.P., and M.S.A. edited the first draft. S.W. edited the manuscript to the final version. All authors contributed to the article and approved the manuscript. **Competing interests:** The authors declare that they have no competing interests. **Data and materials availability:** All data needed to evaluate the conclusions in the paper are present in the paper and/or the Supplementary Materials.

Submitted 23 May 2023
Accepted 3 October 2023
Published 3 November 2023
10.1126/sciadv.adi7347

ScienceAdvances

Copper drives prion protein phase separation and modulates aggregation

Mariana Juliani do Amaral, Satabdee Mohapatra, Aline Ribeiro Passos, Taiana Sousa Lopes da Silva, Renato Sampaio Carvalho, Marcius da Silva Almeida, Anderson Sá Pinheiro, Susanne Wegmann, and Yraima Cordeiro

Sci. Adv. **9** (44), eadi7347. DOI: 10.1126/sciadv.adi7347

Science Advances (ISSN 2375-2548) is published by the American Association for the Advancement of Science. 1200 New York Avenue NW, Washington, DC 20005. The title *Science Advances* is a registered trademark of AAAS.